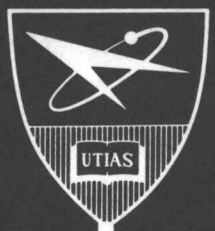

INSTITUTE
FOR
AEROSPACE STUDIES

UNIVERSITY OF TORONTO

PREDICTION OF TWO-DIMENSIONAL TIME-DEPENDENT GASDYNAMIC FLOWS FOR HYPERSONIC STUDIES

by

D. F. Hawken† and J. J. Gottlieb

†Viatec Resource Systems Inc
Toronto, Ontario

March 1990

UTIAS Report No. 335
CN ISSN 0082–5255

PREDICTION OF TWO-DIMENSIONAL TIME-DEPENDENT GASDYNAMIC FLOWS FOR HYPERSONIC STUDIES

by

D. F. Hawken[†] and J. J. Gottlieb

[†]Viatec Resource Systems Inc
Toronto, Ontario

Submitted January 1990

March 1990

UTIAS Report No. 335
CN ISSN 0082–5255

Abstract

Work on the development of an efficient and accurate computer code for the prediction of hypersonic flows within model hypersonic inlets is reported, and numerical results for some test problems are presented. This report summarizes the finite-difference technique and total variation diminishing (TVD) scheme with Roe's approximate Riemann solver, which are incorporated into the code, in order to predict nonstationary planar and axisymmetric flows with steep shocks and thin slip streams on two-dimensional grids having multiple connected domains.

Acknowledgements

The financial support from the Ontario Government University Research Incentive Fund (Award No. TO–4–013) is gratefully acknowledged. We would also like to thank Mr. L. Secord (Viatec Resource Systems Inc.) and Professor R. C. Tennyson (Director, UTIAS) for their interest in this study.

The use of the CRAY supercomputer at the Ontario Centre of Large-Scale Computing was essential to the completion of this work, and we would like to thank the staff at OCLSC for their help.

Table of Contents

1.0 INTRODUCTION

The purpose of this paper is to summarize work done on nonstationary two-dimensional computational fluid dynamics calculations within the joint hypersonic gasdynamics group (Viatec Resource Systems Inc, UTIAS, Ryerson Polytechnical Institute) at the University of Toronto Institute for Aerospace Studies (UTIAS). The aim of this CFD project is to eventually develop a code that will have the capability of computing nonstationary viscous gas flow through or around the models of space-plane inlets that are being tested in the hypersonic impulse tunnel located at UTIAS.

2.0 CURRENT STATUS OF THE CFD CODE

As a preliminary stage, a code has been developed that will compute inviscid planar and axisymmetric flows on two-dimensional grids. The code solves the Euler equations for calorically and thermally perfect gas flow, transformed from a physical domain having curved boundaries to a computational domain subdivided into square cells. Algebraic stretching functions control the physical distribution of the grid lines. The code computes the approximate solution of a Riemann problem as one stage in the solution of the transformed Euler equations. The algorithm of Roe [1] is used as the Riemann problem solver and is implemented so as to compute first-order-accurate fluxes on a rectangular grid. A second-order-accurate flux-limited correction is added to the first-order-accurate flux. Use of the flux limiter to reduce the accuracy towards first order near steep transitions prevents development of oscillations typical of conventional second-order-accurate calculations. Our early work was modelled after the TVD (total variation diminishing) scheme of Chakravarthy [2] and use was made of the work of Yee [3] during the later stages of code development. A description of TVD and related schemes will be given in the following sections. The paper is not intended to be a comprehensive survey of TVD methods, so emphasis will be placed on schemes which have proven useful during development of the TVD code.

In order to predict the flows about model inlets inserted into the hypersonic impulse tunnel at UTIAS, it is necessary to solve problems on multiply-connected domains. The code has been constructed so that the grid may be divided into several subgrids. Time-stepping is executed on each subgrid in turn. The highly vectorized algorithm is applied to an entire column of cells at a time. At present, it is possible to specify four types of boundary conditions at the edges of a subgrid. The boundary condition types are as follows: (1) symmetry of energy, density, and parallel gas flow, and antisymmetry of perpendicular gas flow (i.e., at the walls of an inlet); (2) reflectionless transmission of disturbances at the edge of the computed flow field; (3) supersonic inflow; and (4) continuation of the solution from an adjacent subgrid.

The code has been implemented on the CRAY X-MP/24 at the Ontario Centre for Large Scale Computation, at the University of Toronto. A number of test problems have been solved using explicit or implicit time-stepping with good results. A detailed description of the construction and behaviour of the various versions of the code is contained in sections 5.0 through 10.0.

3.0 SOME CLASSICAL FINITE-DIFFERENCE TECHNIQUES

TVD techniques are most simply introduced when applied to a one-dimensional scalar partial differential equation (PDE). Extension to a system of partial differential equations (the Euler equations) on a two-dimensional domain will be discussed in section 5.0.

It is illuminating to consider the application on a one-dimensional domain of a number of classical finite-difference techniques to a scalar partial difference equation of the form

$$\frac{\partial U}{\partial t} + \frac{\partial f}{\partial X} = 0\,, \tag{1}$$

where U is the solution, t is time, X is the spatial coordinate, and the flux $f = f(U)$ is a function, possibly nonlinear, of U. If the PDE contains viscous terms then f is also a function of spatial derivatives of U. This PDE is in conservation-law form. The general definition of conservation-law form, applicable to systems of PDE's, is that coefficients external to the derivatives are constant, or, if they are variable, their derivatives appear nowhere in the system of PDE's. This conservation-law form is, in fact, an expression, in differential format, of the conservation of some quantity (i.e., mass, momentum, energy). In many cases (see the discussion on shock capturing in Anderson, Tannehill, and Pletcher [4]) it has been shown that conservation-law form will cause the solution of an inviscid equation, that was obtained by removing the second order derivatives from a (physically more accurate) viscid equation, to converge to the solution of the original viscid equation.

It is often desirable to use the conservation-law form when applying a finite-difference algorithm. Assume that the domain has been subdivided into N equal intervals of size ΔX. The intervals (or cells) are centered at $X = i\Delta X - \frac{1}{2}\Delta X$ where i varies from 1 to N. A conservation-law finite-difference algorithm can be constructed by obtaining an approximation to f at the interface between each cell; that is, at $X = i\Delta X$ where i varies from 0 to N. The interface between cell i and cell $i+1$ will be labeled as interface $i + \frac{1}{2}$ in what follows. The boundary interfaces at the left-hand and right-hand sides of the domain will be designated as interface $\frac{1}{2}$ and $N + \frac{1}{2}$, respectively. A difference equation for the solution in the centre of cell i may be written as

$$U_i^{n+1} = U_i^n - \beta\left[F_{i+\frac{1}{2}}^n - F_{i-\frac{1}{2}}^n\right], \tag{2}$$

where $\beta = \Delta t/\Delta X$ is the ratio of the time-step size to the cell width, U_i^n is the numerical solution at node i after the n^{th} time-step, and $F_{i+\frac{1}{2}}^n$ is an approximation to f at the interface between cell i and cell $i+1$ after the n^{th} time-step. $F_{i+\frac{1}{2}}^n$ is an estimate of the flux of U across the interface. Because of the construction of the difference equation, the sum of the fluxes between all the cells is zero. Only the boundary-interface fluxes can contribute to the total flux. That is

$$\sum_{i=1}^{N}\left(F_{i+\frac{1}{2}}^n - F_{i-\frac{1}{2}}^n\right) = F_{N+\frac{1}{2}}^n - F_{\frac{1}{2}}^n\,, \tag{3}$$

In what follows, equation (2) will be said to be in conservative-difference form.

Application of the explicit central-difference method to an inviscid PDE yields an interface flux of the form

$$F_{i+\frac{1}{2}}^n = \frac{f(U_{i+1}^n) + f(U_i^n)}{2}\,. \tag{4}$$

The boundary-interface fluxes may be handled by placing an extra (or image) cell at each end of the domain and assigning a value to U within the extra cell. In some cases known behaviour of the solution outside the domain will supply the value. If this information is not available, imposition of symmetry or antisymmetry about the boundary may supply a suitable value of U or $f(U)$ in the image cell. Extrapolation from the interior of the domain

with the application of analytical relationships is also used, but it can lead to instabilities. Implementation of boundary conditions will be discussed in greater detail at the end of this section and at the end of section 5.0.

The spatial-truncation error of the explicit central-difference method is second-order while the time-truncation error is first-order. If the linear wave equation

$$\frac{\partial U}{\partial t} = -C\frac{\partial U}{\partial X}, \tag{5}$$

where C is a characteristic velocity of propagation, is to be solved, then f is equal to CU. It can be shown that the explicit central-difference method is unconditionally unstable when applied to the linear wave equation. That is, any error in the numerical estimate of U will grow from time-step to time-step. In general, the explicit central-difference method is unconditionally unstable when applied to a PDE that does not contain viscous terms. It does however form a useful basis for methods that add an artificial or numerical viscosity term to the explicit central-difference term. These methods include the TVD algorithms to be discussed later.

An algorithm that is conditionally stable, when applied to the linear wave equation, is the first-order upwind scheme. This method applied to an inviscid PDE results in an interface flux of the form

$$F^n_{i+\frac{1}{2}} = \frac{f(U^n_{i+1}) + f(U^n_i)}{2} - \frac{\sigma_{i+\frac{1}{2}}}{2}\left[f(U^n_{i+1}) - f(U^n_i)\right], \tag{6}$$

where $\sigma_{i+\frac{1}{2}}$ is the sign of the (scalar valued) Jacobian of the interface flux (i.e., derivative of f with respect to U) evaluated at interface $i+\frac{1}{2}$. The Jacobian of the interface flux will be designated by $\lambda_{i+\frac{1}{2}}$ in what follows. $\sigma_{i+\frac{1}{2}}$ is equal to $+1$ if $\lambda_{i+\frac{1}{2}}$ is positive, and it equals -1 otherwise. In order to keep in mind the scalar nature of the present equations and to be consistent with the use of vector-valued fluxes in work to be described in section 5.0, $\lambda_{i+\frac{1}{2}}$ will also be called the interface-flux eigenvalue.

In the case of the linear wave equation, the interface flux reduces to the form

$$F^n_{i+\frac{1}{2}} = \frac{C - |C|}{2}U^n_{i+1} + \frac{C + |C|}{2}U^n_i. \tag{7}$$

In other words, backward differences are used if the "wind," C, is positive, and forward differences otherwise. The error will not grow with time if the CFL condition condition $|C\beta| \leq 1$ is satisfied. Unfortunately, the spatial truncation error is only first order.

A method in which the truncation error is second order in both space and time, is the explicit algorithm of MacCormack [5]. This method consists of the predictor step

$$\breve{U}^n_i = U^n_i - \beta[f(U^n_i) - f(U^n_{i-1})], \tag{8}$$

followed by the corrector step

$$U^{n+1}_i = U^n_i + \frac{1}{2}\left[\breve{U}^n_i - U^n_i - \beta[f(\breve{U}^n_{i+1}) - f(\breve{U}^n_i)]\right]. \tag{9}$$

If the solution contains a shock wave, a slightly better result occurs if the predictor differencing is in the upwind direction followed by downwind differencing in the corrector. Thus,

in some cases there is an advantage to using forward differences in the predictor followed by backward differences in the corrector. In more complex cases, the direction of differencing is alternated from time-step to time-step in order to eliminate any bias. Examination of the corrector equation reveals that an interface flux can be written as

$$F^n_{i+\frac{1}{2}} = \frac{f(\breve{U}^n_{i+1}) + f(U^n_i)}{2}. \tag{10}$$

A method closely related to the algorithm of MacCormack is that of Lax-Wendroff [6]. The methods have the same truncation error in time and space. The methods are identical when applied to the linear wave equation; the solution is stable if the CFL condition $|C\beta| \leq 1$ is satisfied. The Lax-Wendroff method may be written in the form

$$\begin{aligned} U^{n+1}_i &= U^n_i - \frac{\beta}{2}[f(U^n_{i+1}) - f(U^n_{i-1})] \\ &\quad + \frac{\beta^2}{2}\Big[\, \lambda_{i+\frac{1}{2}}[f(U^n_{i+1}) - f(U^n_i)\,] + \lambda_{i-\frac{1}{2}}[f(U^n_i) - f(U^n_{i-1})\,]\,\Big]. \end{aligned} \tag{11}$$

The last term is a thinly disguised central-difference approximation to a second-order spatial derivative and amounts to the inclusion of an artificial viscosity term.

The interface flux for the Lax-Wendroff method may be written

$$F^n_{i+\frac{1}{2}} = \frac{f(U^n_{i+1}) + f(U^n_i)}{2} - \beta\frac{\lambda_{i+\frac{1}{2}}}{2}\Big[f(U^n_{i+1}) - f(U^n_i)\Big]. \tag{12}$$

In fact, this is just a first-order Taylor expansion about U^n_{i+1} of the MacCormack interface flux.

In the case of the linear wave equation, the interface flux reduces to the form

$$F^n_{i+\frac{1}{2}} = \frac{C - \beta C^2}{2}U^n_{i+1} + \frac{C + \beta C^2}{2}U^n_i. \tag{13}$$

For the linear wave equation, it is evident that the Lax-Wendroff interface flux reduces to the first-order upwind interface flux when $|C\beta|$ is unity. If $|C\beta|$ is close to zero, the interface flux of the (unconditionally unstable) explicit central-difference method is approximated. Intermediate values of $|C\beta|$ yield a mixture of central and first-order upwind differences. For nonlinear problems, the Lax-Wendroff and MacCormack methods give the most accurate results when β is chosen so that the CFL limit of one is approached; the leading coefficient of the truncation error approaches zero as $|C\beta|$ approaches unity.

Examination of the interface fluxes for the first-order upwind, MacCormack, and Lax-Wendroff methods reveals that they consist of the interface flux for the explicit central-difference method plus some extra terms. These extra terms amount to the addition of artificial or numerical viscosity to the difference equations. There are many other difference methods which can also be written in the form of the explicit central-difference method with additional artificial viscosity terms.

The first-order upwind method is the most effective in eliminating oscillations near shocks; the solution of the linear wave equation is always monotone near a shock. However, the shock thickness is much larger than that obtained if a higher order method is used. Unfortunately, as proven by Harten, Hyman and Lax [7], no higher-order classical finite-difference method can produce monotone shocks.

Many of the methods use extra information about the solution, obtained by examining the interface-flux Jacobian, to modify the interface fluxes. In the case of systems of PDE's, the solution characteristics (or eigenvalues of the Jacobian vector of the fluxes) are examined. Note that, if f is nonlinear, the Jacobian and therefore the coefficients of f in the expressions for the interface fluxes may vary from interface to interface. In one sense, the conservation-law form of equation (1) has been compromised. However, the closely related property of satisfying equation (3) has been retained.

A commonly used spatially zero-order accurate means of imposing a transmission boundary condition is applied by requiring that the value of U in the image cell be set to the value of U in the real cell directly adjacent to the boundary (i.e., the first derivative of U is set to zero at the boundary). This is denoted as "constant extrapolation" by Kamowitz [8]. Kamowitz has investigated the passage of a shock-like solution structures through transmissive boundaries. He computed the numerical solution of a number of one-dimensional scalar test equations problems (in which U represented a velocity of propagation) using the MacCormack, Lax-Wendroff and similar schemes. Kamowitz showed that if constant extrapolation was used the shocks exited through the boundary without disturbing the solution within the domain of calculation.

Since the Lax-Wendroff and MacCormack schemes are spatially second-order accurate, it is desirable to also use a transmission boundary condition of greater than zero-order accuracy. If higher order extrapolation of U was used (i.e., the second or third derivative of U is set to zero at the boundary) then the shock was properly transmitted if f was a linear function of U, but a nonlinear f resulted in the creation of boundary layers or reflected shocks. The combination of nonlinear f and higher-order extrapolation caused the value of U at the real cell adjacent to the boundary to remain zero or to have an inappropriate sign during the outward propagation of the shock.

Kamowitz recommended the use of characteristic extrapolation as a means of obtaining both a first-order accurate boundary condition and acceptable transmission of shock waves. In the context of this report, the scheme involves the storage of image-cell values U_0 and U_{N+1} which are updated before the start of each time-step using the relations

$$U_0^{n+1} = U_0^n - \beta[f(U_1^n) - f(U_0^n)] \tag{14}$$

and

$$U_{N+1}^{n+1} = U_{N+1}^n - \beta[f(U_{N+1}^n) - f(U_N^n)]\,, \tag{15}$$

respectively.

4.0 TVD METHODS APPLIED TO A SCALAR EQUATION

Use of the solution characteristics has proven to be a desirable ingredient in improving solution quality. The TVD methods examine additional solution properties in order to modify the interface flux so that it reduces to the first-order upwind interface flux in regions of rapid solution variation but is of higher order accuracy elsewhere. A very simple TVD interface flux may be written in the form

$$\begin{aligned} F_{i+\frac{1}{2}}^n = {} & \frac{f(U_{i+1}^n) + f(U_i^n)}{2} - \frac{\sigma_{i+\frac{1}{2}}}{2}\left[f(U_{i+1}^n) - f(U_i^n)\right] \\ & + \frac{\sigma_{i+\frac{1}{2}}}{2}\text{minmod}(\Delta f_{i+\frac{3}{2}}^-, \Delta f_{i+\frac{1}{2}}^-) + \frac{\sigma_{i+\frac{1}{2}}}{2}\text{minmod}(\Delta f_{i+\frac{1}{2}}^+, \Delta f_{i-\frac{1}{2}}^+)\,. \end{aligned} \tag{16}$$

Using the notation $\sigma^{\pm}_{i+\frac{1}{2}} = [\sigma_{i+\frac{1}{2}} \pm 1]/2$, the quantity

$$\Delta f^{+}_{i+\frac{1}{2}} = \sigma^{+}_{i+\frac{1}{2}} \left[f(U^n_{i+1}) - f(U^n_i) \right] \tag{17}$$

is equal to the flux difference at interface $i+\frac{1}{2}$, if the interface-flux eigenvalue is positive, and it is equal to zero otherwise. The closely related quantity

$$\Delta f^{-}_{i+\frac{1}{2}} = -\sigma^{-}_{i+\frac{1}{2}} \left[f(U^n_{i+1}) - f(U^n_i) \right] \tag{18}$$

is equal to the flux difference at interface $i+\frac{1}{2}$ if the interface-flux eigenvalue is negative, and it is equal to zero otherwise. The function 'minmod', originally introduced by Roe and described in Sweby [9], is defined by

$$\text{minmod(a,b)} = \begin{cases} 0 & \text{if } ab < 0, \\ a & \text{if } |a| \le |b|, \\ b & \text{if } |b| \le |a|. \end{cases} \tag{19}$$

In other words, 'minmod' returns the argument of least magnitude unless the arguments are of different sign, in which case it is zero.

The first two terms in equation (16) comprise the first-order accurate upwind interface flux at interface $i+\frac{1}{2}$. The last two terms will cancel the second term to yield the spatially second-order accurate explicit central-difference interface flux under the following condition: the flux difference at interface $i+\frac{1}{2}$ does not exceed the flux difference at the interface in the upwind direction from interface $i+\frac{1}{2}$ and is of the same sign. If this condition is violated and the flux differences are of the same sign there is only a partial cancellation of the second term in equation (16). The first-order upwind interface flux is retained if the flux differences are of opposite sign. Only the upwind interface has an influence because of the design of the last two terms in equation (16). Many other "flux limiters" besides minmod have been designed and are discussed, for example, in Yee [3].

If the last three terms in equation (16) are linearized with respect to U and a few simplifying approximations are made, a nearly equivalent formulation may be written in terms of the differences of U across an interface. The result is

$$\begin{aligned} F^n_{i+\frac{1}{2}} = {} & \frac{f(U^n_{i+1}) + f(U^n_i)}{2} - \frac{|\lambda_{i+\frac{1}{2}}|}{2} \Delta U^n_{i+\frac{1}{2}} \\ & - \frac{\lambda^{-}_{i+\frac{1}{2}}}{2} \text{minmod}(\Delta U^n_{i+\frac{3}{2}}, \Delta U^n_{i+\frac{1}{2}}) + \frac{\lambda^{+}_{i+\frac{1}{2}}}{2} \text{minmod}(\Delta U^n_{i+\frac{1}{2}}, \Delta U^n_{i-\frac{1}{2}}), \end{aligned} \tag{20}$$

where

$$\Delta U^n_{i+\frac{1}{2}} = U^n_{i+1} - U^n_i \qquad \text{and} \qquad \lambda^{\pm}_{i+\frac{1}{2}} = \frac{\lambda_{i+\frac{1}{2}} \pm |\lambda_{i+\frac{1}{2}}|}{2}. \tag{21}$$

Use of equation (20) instead of equation (16) results in a smaller operation count since fewer flux functions need be evaluated. In this case, the degree of cancellation of the second term by the last two terms depends on the relative sizes of the difference of U across interface $i+\frac{1}{2}$ and the difference of U across the upwind interface.

Chakravarthy [2] has evolved a more flexible, but more complex, scheme in which the interface flux may be written in the form

$$F^n_{i+\frac{1}{2}} = \frac{f(U^n_{i+1}) + f(U^n_i)}{2} - \frac{|\lambda_{i+\frac{1}{2}}|}{2}\Delta U^n_{i+\frac{1}{2}}$$
$$- \lambda^-_{i+\frac{1}{2}}\left(\frac{1-\theta}{4}\text{minmod}(\Delta U^n_{i+\frac{3}{2}}, \omega\Delta U^n_{i+\frac{1}{2}}) + \frac{1+\theta}{4}\text{minmod}(\omega\Delta U^n_{i+\frac{3}{2}}, \Delta U^n_{i+\frac{1}{2}})\right)$$
$$+ \lambda^+_{i+\frac{1}{2}}\left(\frac{1+\theta}{4}\text{minmod}(\Delta U^n_{i+\frac{1}{2}}, \omega\Delta U^n_{i-\frac{1}{2}}) + \frac{1-\theta}{4}\text{minmod}(\omega\Delta U^n_{i+\frac{1}{2}}, \Delta U^n_{i-\frac{1}{2}})\right). \quad (22)$$

Equation (22) is identical to equation (20) if the compression parameter, ω, is set equal to unity, regardless of the value of θ.

Steeper shocks are obtained if ω is set to a value larger than unity. In sufficiently smooth regions, the last two terms cancel the second term so as to produce a higher-order interface flux. The specific difference scheme that results is determined by the value of θ, and it is stable if ω is within the limits given by

$$0 < \omega \leq \frac{3-\theta}{1-\theta}, \quad (23)$$

and if the time-step size is controlled such that the Courant number is less than

$$\frac{4}{5-\theta+\omega(1+\theta)}. \quad (24)$$

A number of special cases have been analyzed by Chakravarthy [2]. If θ equals $+1$, the scheme is central differences and ω has no limit. If the value of θ is -1 the scheme is fully upwind and ω must be less than 2. A value of $-\frac{1}{3}$ for θ yields the requirement that ω be less than $\frac{5}{2}$, while a limit for ω of 3 results if θ equals 0. The smallest truncation error occurs if θ is set to $\frac{1}{2}$, in which case ω must be smaller than 5 for stability. All the previously listed values of θ result in formally second-order accurate schemes. If θ is given the value of $\frac{1}{3}$ a third-order accurate steady-state solution scheme is obtained, in which ω is constrained to be less than four. It is usually better to use a value of ω that is less than the permitted value, partly because the resultant allowed Courant number is larger and partly because the limits on ω were obtained by means of a linear analysis.

The case $\theta = 1$ warrants further study. The resultant interface flux is identical to that in equation (20) except for the presence of ω. The condition for cancellation of the second term in equation (22) becomes: ΔU at interface $i+\frac{1}{2}$ does not exceed the product of ω and ΔU at the interface in the upwind direction from interface $i+\frac{1}{2}$ and is of the same sign. If ω exceeds 1, the result is greater compression of transitions. Conversely, if ω is less than one, the result is reduced compression of transitions and ultimately the first-order upwind method is reproduced for ω equal to zero.

A somewhat different TVD method based on the Lax-Wendroff differencing scheme was employed by Roe, described more clearly in Roe and Pike [10] and most clearly in Sweby [9]. It may be written as

$$U^{n+1}_i = U^n_i - \beta\lambda^-_{i+\frac{1}{2}}\Delta U^n_{i+\frac{1}{2}} - \beta\lambda^+_{i-\frac{1}{2}}\Delta U^n_{i-\frac{1}{2}} - \beta\left[\Phi^n_{i+\frac{1}{2}} - \Phi^n_{i-\frac{1}{2}}\right], \quad (25)$$

where $\Phi^n_{i+\frac{1}{2}}$ is defined by

$$\Phi^n_{i+\frac{1}{2}} = \sigma^-_{i+\frac{1}{2}}\text{minmod}(\Delta h^n_{i+\frac{3}{2}}, \Delta h^n_{i+\frac{1}{2}}) + \sigma^+_{i+\frac{1}{2}}\text{minmod}(\Delta h^n_{i+\frac{1}{2}}, \Delta h^n_{i-\frac{1}{2}}), \tag{26}$$

where in turn

$$\Delta h^n_{i+\frac{1}{2}} = \frac{1-\beta|\lambda_{i+\frac{1}{2}}|}{2}\lambda_{i+\frac{1}{2}}[U^n_{i+1} - U^n_i]. \tag{27}$$

If the solution is sufficiently smooth, the $\Phi^n_{i\pm\frac{1}{2}}$ terms will be nonzero and will act, to some degree, to convert the interface flux to that of the spatially and temporally second-order accurate Lax-Wendroff method in linearized form. Otherwise, the first-order upwind interface flux is obtained.

Inspection of the first line of equation (25) reveals that it is not in conservative-difference form. A closely related TVD method which is in conservative-difference form may be written if the interface flux is defined by

$$F^n_{i+\frac{1}{2}} = \frac{f(U^n_{i+1}) + f(U^n_i)}{2} - \frac{|\lambda_{i+\frac{1}{2}}|}{2}\Delta U^n_{i+\frac{1}{2}} + \Phi^n_{i+\frac{1}{2}}. \tag{28}$$

Here $\Phi^n_{i+\frac{1}{2}}$ may be defined as above or may be simplified to yield the nearly equivalent expression

$$\Phi^n_{i+\frac{1}{2}} = \frac{|\lambda_{i+\frac{1}{2}}| - \beta(\lambda_{i+\frac{1}{2}})^2}{2}Q^n_{i+\frac{1}{2}}, \tag{29}$$

using the limiter term

$$Q^n_{i+\frac{1}{2}} = -\sigma^-_{i+\frac{1}{2}}\text{minmod}(\Delta U^n_{i+\frac{3}{2}}, \Delta U^n_{i+\frac{1}{2}}) + \sigma^+_{i+\frac{1}{2}}\text{minmod}(\Delta U^n_{i+\frac{1}{2}}, \Delta U^n_{i-\frac{1}{2}}). \tag{30}$$

Yee [3] advocates an operator splitting approach that uses TVD differencing as a post-processor after application of the MacCormack scheme. She recommends the use of the MacCormack scheme as an efficient means of including source terms ($S_i = S(U_i, X_i)$), especially when the method is extended to the solution of multidimensional problems. The equations may be expressed as a predictor step

$$\check{U}^n_i = U^n_i - \beta[f(U^n_i) - f(U^n_{i-1})] - \Delta t\, S_i, \tag{31}$$

followed by the MacCormack corrector step

$$\tilde{U}^{n+1}_i = U^n_i + \frac{1}{2}\Big[\ \check{U}^n_i - U^n_i - \beta\Big[f(\check{U}^n_{i+1}) - f(\check{U}^n_i)\Big]\ \Big] - \Delta t\, \hat{S}_i, \tag{32}$$

which in turn is followed by the TVD post-processor

$$U^{n+1}_i = \tilde{U}^n_i - \beta\Big[\tilde{\Phi}^n_{i+\frac{1}{2}} - \tilde{\Phi}^n_{i-\frac{1}{2}}\Big], \tag{33}$$

where

$$\tilde{\Phi}^n_{i+\frac{1}{2}} = \frac{|\tilde{\lambda}_{i+\frac{1}{2}}| - \beta(\tilde{\lambda}_{i+\frac{1}{2}})^2}{2}\Big[\tilde{Q}^n_{i+\frac{1}{2}} - \Delta\tilde{U}^n_{i+\frac{1}{2}}\Big]. \tag{34}$$

The quantity within the final set of brackets is zero in regions where the solution is sufficiently smooth, owing to the action of the limiter term, $\tilde{Q}^n_{i+\frac{1}{2}}$ which, to be consistent with

the upwind weighting of previous equations may be defined as in equation (30). In regions where the solution is insufficiently smooth, $\tilde{\Phi}^n_{i+\frac{1}{2}}$ tends to replace the Lax-Wendroff-like interface flux of the MacCormack method with the interface flux of the first-order upwind method. Yee [3] advocates the use of a symmetric, or nonupwind weighted, limiter term in equation (33) (and in equation (29)), which in this case might take such forms as

$$\tilde{Q}^n_{i+\frac{1}{2}} = \text{minmod}(\Delta\tilde{U}^n_{i+\frac{3}{2}}, \Delta\tilde{U}^n_{i+\frac{1}{2}}) + \text{minmod}(\Delta\tilde{U}^n_{i+\frac{1}{2}}, \Delta\tilde{U}^n_{i-\frac{1}{2}}) - \Delta\tilde{U}^n_{i+\frac{1}{2}} \tag{35}$$

or

$$\tilde{Q}^n_{i+\frac{1}{2}} = \text{minmod}\left(\Delta\tilde{U}^n_{i+\frac{1}{2}}, \text{minmod}(\Delta\tilde{U}^n_{i+\frac{3}{2}}, \Delta\tilde{U}^n_{i-\frac{1}{2}})\right). \tag{36}$$

Use of symmetric limiter terms results in a lower operations count at the cost of a slight degeneration in quality.

There are a large number of additional TVD formulations which cannot be discussed here, owing to lack of space. However, many are treated in detail by Yee [3] along with various forms of limiter terms.

5.0 APPLICATION OF TVD METHOD TO EULER EQUATIONS

It is convenient to write the inviscid equations of gasdynamics in terms of the time derivatives of four conserved quantities E, ρ, ρU, and ρV on a two-dimensional spatial domain with coordinates X and Y. E is the total energy of the gas per unit volume, ρ is the gas density, and U and V are the gas velocities in the X and Y directions, respectively. The spatial domain is essentially rectangular in shape but may have curved or sloping boundaries. The inviscid gasdynamical equations in planar or axisymmetric form may be expressed in vector form as follows:

$$\frac{\partial \underline{U}}{\partial t} + \frac{\partial \underline{f}}{\partial X} + \frac{\partial \underline{h}}{\partial Y} + \underline{S} = 0. \tag{37}$$

$\underline{U}$ is a column vector which contains the four components of the solution and is defined by

$$\underline{U} = [E \quad \rho \quad \rho U \quad \rho V]^T, \tag{38}$$

where T is the transpose operator. $\underline{f}$ and $\underline{h}$ are the vector valued fluxes along the X and Y directions, respectively. They are defined as

$$\underline{f} = \left[EU + PU \quad \rho U \quad \rho U^2 + P \quad \rho UV\right]^T, \tag{39}$$

$$\underline{h} = \left[EV + PV \quad \rho V \quad \rho UV \quad \rho V^2 + P\right]^T, \tag{40}$$

where the pressure, P, may be computed from the components of $\underline{U}$ using the formula

$$P = (\gamma - 1)\left[E - \frac{(\rho U)^2 + (\rho V)^2}{2\rho}\right], \tag{41}$$

for the case of a perfect gas, where γ is the specific heat ratio. $\underline{S}$ is a source term which is zero if the problem to be solved uses Cartesian coordinates. If an axisymmetric problem is to be solved, $\underline{S}$ is given by

$$\underline{S} = \left[\frac{E+P}{Y}V \quad \frac{\rho V}{Y} \quad \frac{\rho UV}{Y} \quad \frac{\rho V^2}{Y}\right]^T. \tag{42}$$

In the above column vector, it is assumed that the X axis is the axis of symmetry and that Y is the radius about the X axis.

It is convenient to transform these equations from the spatial domain with coordinates X and Y, to a rectangular computational domain with coordinates ξ and η. The Jacobian of the transformation, J, which is a scalar function of the first-order partial derivatives of X and Y with respect ξ and η, is defined by

$$\frac{1}{J} = X_\xi Y_\eta - X_\eta Y_\xi \,. \tag{43}$$

It is also useful to introduce a notation where X_ξ is the partial derivative of X with respect to ξ at constant η and t, and X_η is the partial derivative of X with respect to η at constant ξ and t. The partial derivatives Y_ξ and Y_η have analogous definitions.

The transformed Euler equations may be written

$$\frac{\partial \bar{U}}{\partial t} + \frac{\partial \bar{f}}{\partial \xi} + \frac{\partial \bar{h}}{\partial \eta} + \bar{S} = 0 \,, \tag{44}$$

where any quantity with an overhead bar is a column vector that has the factor J in its denominator. More specifically, $\bar{U} = \underline{U}/J$, $\bar{f} = \underline{f}\xi_x/J + \underline{h}\xi_y/J$, $\bar{h} = \underline{f}\eta_x/J + \underline{h}\eta_y/J$, and $\bar{S} = \underline{S}/J$. The quantities ξ_x, ξ_y, η_x, and η_y are the partial derivatives of ξ and η with respect to X or Y. The identities $\xi_x/J = Y_\eta$, $\xi_y/J = -X_\eta$, $\eta_x/J = -Y_\xi$, and $\eta_y/J = X_\xi$ facilitate calculation of metrics in the computational frame. The transformed vector-valued equation originally contains the additional terms $\underline{f}[Y_{\xi\eta} - Y_{\eta\xi}]$ and $\underline{h}[X_{\eta\xi} - X_{\xi\eta}]$ but the extra terms are are identically zero because the second-order derivatives satisfy the identities $Y_{\xi\eta} = Y_{\eta\xi}$ and $X_{\xi\eta} = X_{\eta\xi}$. As discussed in detail by Thomas and Lombard [11], it is crucial to select the differencing method so that the two identities still hold when the metrics are approximated by finite differences. Violation of the two identities results in the effective introduction of an extra source term and would cause nonconservation of the free stream.

The scalar TVD formulation must be modified to deal with the vector nature of the PDE's. Equation (44) without the source term may be linearized to obtain

$$\frac{\partial \bar{U}}{\partial t} + \left[\frac{\partial \bar{f}}{\partial \bar{U}}\right]\frac{\partial \bar{U}}{\partial \xi} + \left[\frac{\partial \bar{h}}{\partial \bar{U}}\right]\frac{\partial \bar{U}}{\partial \eta} = 0 \,. \tag{45}$$

$[\partial \bar{f}/\partial \bar{U}]$ is a four by four matrix whose components are the derivatives of the components of $\bar{f}$ with respect to the components of $\bar{U}$ and will be called the Jacobian of $\bar{f}$. Similarly, $[\partial \bar{h}/\partial \bar{U}]$ will be denoted the Jacobian of $\bar{h}$. The TVD fluxes are are expressed as weighted sums of the eigenvectors of the Jacobians. The size and sign of the weights depend on the smoothness of the solution and on the four eigenvalues of each Jacobian matrix, in a manner that will be detailed later.

In order to discretize the transformed equations, the rectangular computational domain is divided into square cells by vertical and horizontal lines with unit spacing. It is convenient to label the cells with the index pair i,k such that i equals one along the left-most column of cells and increases to the right, whereas k equals one along the bottom row of cells and increases upwards. The values of ξ and η at the centre of cell i,k are $\xi_{i,k} = i$ and $\eta_{i,k} = k$, respectively. The four corners of cell i,k have numerical coordinates $i \pm \frac{1}{2}, k \pm \frac{1}{2}$. The square cells are mapped onto, possibly deformed, rectangles in the spatial coordinate

system. Using the above definition of ξ and η the transformed equations are discretized at each cell i,k to obtain the difference equation

$$\underline{U}_{i,k}^{n+1} - \underline{U}_{i,k}^{n} = -\beta_{i,k}\left[\bar{F}_{i+\frac{1}{2},k}^{n} - \bar{F}_{i-\frac{1}{2},k}^{n}\right] - \beta_{i,k}\left[\bar{H}_{i,k+\frac{1}{2}}^{n} - \bar{H}_{i,k-\frac{1}{2}}^{n}\right] - \beta_{i,k}\bar{S}_{i,k}^{n}, \qquad (46)$$

where $\beta_{i,k}$ is the value of $J\Delta t$ evaluated at the centre of cell i,k and $\bar{F}_{i+\frac{1}{2},k}^{n}$ is a numerical estimate of the flux through the right-hand interface of cell i,k evaluated at time level n and has the form

$$\bar{F}_{i+\frac{1}{2},k}^{n} = \frac{\underline{f}(\underline{U}_{i+1,k}^{n}) + \underline{f}(\underline{U}_{i,k}^{n})}{2}\hat{\Omega}_x + \frac{\underline{h}(\underline{U}_{i+1,k}^{n}) + \underline{h}(\underline{U}_{i,k}^{n})}{2}\hat{\Omega}_y - \sum_{m=1}^{4} W_{i+\frac{1}{2},k}^{m}\underline{R}_{i+\frac{1}{2},k}^{m}. \qquad (47)$$

$\hat{\Omega}_x = \xi_x/J$ and $\hat{\Omega}_y = \xi_y/J$ evaluated at $i+\frac{1}{2},k$ (i.e., $\hat{\Omega}_x = Y_{i+\frac{1}{2},k+\frac{1}{2}} - Y_{i+\frac{1}{2},k-\frac{1}{2}}$ and $\hat{\Omega}_y = X_{i+\frac{1}{2},k-\frac{1}{2}} - X_{i+\frac{1}{2},k+\frac{1}{2}}$) incorporate the effect of the length and orientation of the right-hand interface of cell i,k on the flux.

If only the first two terms in the expression for the interface flux were present, the explicit central-difference method would be obtained. The last term adds numerical viscosity to the first two terms to produce the first-order upwind method except when the solution is sufficiently smooth. The last term is the weighted summation the four eigenvectors of the Jacobian of $\underline{f}\xi_x/J + \underline{h}\xi_y/J$ evaluated at the right-hand interface of cell i,k. After Chakravarthy [2], it is convenient to define a four by four matrix [R] whose columns are the eigenvectors. That is,

$$[R] = \begin{bmatrix} \frac{Q^2}{2C} - U_c + \frac{C}{\gamma-1} & \frac{Q^2}{2C} + V_c & \frac{Q^2}{2C} - V_c & \frac{Q^2}{2C} + U_c + \frac{C}{\gamma-1} \\ \frac{1}{C} & \frac{1}{C} & \frac{1}{C} & \frac{1}{C} \\ \frac{U}{C} - \Omega_x & \frac{U}{C} - \Omega_y & \frac{U}{C} + \Omega_y & \frac{U}{C} + \Omega_x \\ \frac{V}{C} - \Omega_y & \frac{V}{C} + \Omega_x & \frac{V}{C} - \Omega_x & \frac{V}{C} + \Omega_y \end{bmatrix}, \qquad (48)$$

where $\Omega_x = \hat{\Omega}_x/\sqrt{\hat{\Omega}_x\hat{\Omega}_x + \hat{\Omega}_y\hat{\Omega}_y}$, $\Omega_y = \hat{\Omega}_y/\sqrt{\hat{\Omega}_x\hat{\Omega}_x + \hat{\Omega}_y\hat{\Omega}_y}$, C is the speed of sound, and $Q^2 = U^2 + V^2$, all evaluated at the right-hand interface of cell i,k. $U_c = U\Omega_x + V\Omega_y$ is the flow speed perpendicular to the interface and $V_c = V\Omega_x - U\Omega_y$ is the flow speed parallel to the interface. $\underline{R}_{j+\frac{1}{2},k}^{m}$ has components given by the m^{th} column of $[R]$.

The weights in the summation of equation (47) have the form

$$\begin{aligned} W_{i+\frac{1}{2},k}^{m} = {} & \frac{|\lambda_{i+\frac{1}{2},k}^{m}|}{2}\alpha_{i+\frac{1}{2},k}^{m} \\ & + \lambda_{i+\frac{1}{2},k}^{m-}\left(\frac{1-\theta}{4}\text{minmod}(\alpha_{i+\frac{3}{2},k}^{'m}, \omega\alpha_{i+\frac{1}{2},k}^{m}) + \frac{1+\theta}{4}\text{minmod}(\omega\alpha_{i+\frac{3}{2},k}^{'m}, \alpha_{i+\frac{1}{2},k}^{m})\right) \\ & - \lambda_{i+\frac{1}{2},k}^{m+}\left(\frac{1+\theta}{4}\text{minmod}(\alpha_{i+\frac{1}{2},k}^{m}, \omega\alpha_{i-\frac{1}{2},k}^{'m}) + \frac{1-\theta}{4}\text{minmod}(\omega\alpha_{i+\frac{1}{2},k}^{m}, \alpha_{i-\frac{1}{2},k}^{'m})\right), \end{aligned} \qquad (49)$$

where $\alpha^m_{i+\frac{1}{2},k}$ is the projection of the difference in $\underline{U}$ across interface $i+\frac{1}{2},k$ onto the m^{th} eigenvector. The projection is calculated using

$$\alpha^m_{i+\frac{1}{2},k} = \underline{L}^m_{i+\frac{1}{2},k} \bullet \left[\underline{U}_{i+1,k} - \underline{U}_{i,k}\right]. \tag{50}$$

The projections of the difference in $\underline{U}$ at the interfaces to each side of interface $i+\frac{1}{2},k$ are given by

$$\alpha'^m_{i+\frac{3}{2},k} = \underline{L}^m_{i+\frac{1}{2},k} \bullet \left[\underline{U}_{i+2,k} - \underline{U}_{i+1,k}\right] \qquad \text{and} \qquad \alpha'^m_{i-\frac{1}{2},k} = \underline{L}^m_{i+\frac{1}{2},k} \bullet \left[\underline{U}_{i,k} - \underline{U}_{i-1,k}\right]. \tag{51}$$

The vector $\underline{L}^m_{i+\frac{1}{2},k}$ is given by the m^{th} row of the four by four matrix

$$[L] = \frac{1}{2}\begin{bmatrix} +\frac{\gamma-1}{C} & +\frac{\gamma-1}{2C}Q^2 + U_c & -\frac{\gamma-1}{C}U - \Omega_x & -\frac{\gamma-1}{C}V - \Omega_y \\ -\frac{\gamma-1}{C} & -\frac{\gamma-1}{2C}Q^2 - V_c + C & +\frac{\gamma-1}{C}U - \Omega_y & +\frac{\gamma-1}{C}V + \Omega_x \\ -\frac{\gamma-1}{C} & -\frac{\gamma-1}{2C}Q^2 + V_c + C & +\frac{\gamma-1}{C}U + \Omega_y & +\frac{\gamma-1}{C}V - \Omega_x \\ +\frac{\gamma-1}{C} & +\frac{\gamma-1}{2C}Q^2 - U_c & -\frac{\gamma-1}{C}U + \Omega_x & -\frac{\gamma-1}{C}V + \Omega_y \end{bmatrix}, \tag{52}$$

which is the inverse of $[R]$. Strictly speaking, $\underline{U}_{i+1,k} - \underline{U}_{i,k}$ in equation (50) should be $\bar{U}_{i+1,k} - \bar{U}_{i,k}$, but the missing factor $1/J$ is included in $\lambda^m_{i+\frac{1}{2},k}$, which is the m^{th} eigenvalue of $[\partial \bar{f}/\partial \bar{U}]$ divided by J evaluated at the right-hand interface of cell i,k. The values of $\lambda^m_{i+\frac{1}{2},k}$ that correspond to $\underline{R}^m_{i+\frac{1}{2},k}$ and $\underline{L}^m_{i+\frac{1}{2},k}$ are given by

$$\begin{aligned} \lambda^1_{i+\frac{1}{2},k} &= [U_c - C]\sqrt{\hat{\Omega}_x\hat{\Omega}_x + \hat{\Omega}_y\hat{\Omega}_y}\,, \\ \lambda^2_{i+\frac{1}{2},k} &= \lambda^3_{i+\frac{1}{2},k} = U_c\sqrt{\hat{\Omega}_x\hat{\Omega}_x + \hat{\Omega}_y\hat{\Omega}_y}\,, \\ \lambda^4_{i+\frac{1}{2},k} &= [U_c + C]\sqrt{\hat{\Omega}_x\hat{\Omega}_x + \hat{\Omega}_y\hat{\Omega}_y}\,. \end{aligned} \tag{53}$$

The eigenvalues correspond to characteristics of the system of PDE's. The signs of the eigenvalues at an interface determine the influence of the solution at one cell on the solution at adjacent cells. In what follows the "eigenvalues" will always contain a factor of J in the denominator.

The first and fourth eigenvalues must be adjusted to prevent the development of aphysical shock-like structures in rarefaction waves ("rarefaction shocks") in regions where the flow velocity changes from subsonic to supersonic. A number of "sonic correction" techniques have been used. One of the simplest, described in Yee [3], has been used in this work. Let $|\lambda^{max}|$ be the absolute value of the eigenvalue with maximum magnitude at interface $i+\frac{1}{2},k$ (that is, $|\lambda^{max}| = [|U_c| + C]\sqrt{\hat{\Omega}_x\hat{\Omega}_x + \hat{\Omega}_y\hat{\Omega}_y}$). Then the first and fourth eigenvalues are adjusted using the formula

$$\lambda = \begin{cases} \lambda & \text{if } |\lambda| \geq |\lambda^{max}|\,\delta \\ \dfrac{\lambda^2 + |\lambda^{max}|^2\,\delta^2}{2|\lambda^{max}|\,\delta}\text{sign}(\lambda) & \text{if } |\lambda| < |\lambda^{max}|\,\delta \end{cases}, \tag{54}$$

where δ is a small number ranging from 0.01 to 0.15.

In order to evaluate the eigenvectors and eigenvalues at the interface, an approximation to $\underline{U}$ must be obtained. A very simple approximation is to take the arithmetic average of $\underline{U}$ in the cells to each side. A number of more complex approximations have been used. The approach taken by Chakravarthy [2] and retained herein is to use the averages of Roe [1], which lead to particularly thin shocks. The average density, velocities, enthalpy, and speed of sound are expressed as

$$\rho_{i+\frac{1}{2},k} = \sqrt{\rho_{i+1,k}}\sqrt{\rho_{i,k}}, \tag{55}$$

$$U_{i+\frac{1}{2},k} = \frac{U_{i+1,k}\sqrt{\rho_{i+1,k}} + U_{i,k}\sqrt{\rho_{i,k}}}{\sqrt{\rho_{i+1,k}} + \sqrt{\rho_{i,k}}}, \tag{56}$$

$$V_{i+\frac{1}{2},k} = \frac{V_{i+1,k}\sqrt{\rho_{i+1,k}} + V_{i,k}\sqrt{\rho_{i,k}}}{\sqrt{\rho_{i+1,k}} + \sqrt{\rho_{i,k}}}, \tag{57}$$

$$\varepsilon_{i+\frac{1}{2},k} = \frac{\varepsilon_{i+1,k}\sqrt{\rho_{i+1,k}} + \varepsilon_{i,k}\sqrt{\rho_{i,k}}}{\sqrt{\rho_{i+1,k}} + \sqrt{\rho_{i,k}}}, \tag{58}$$

$$C_{i+\frac{1}{2},k} = \sqrt{\gamma - 1}\sqrt{\varepsilon_{i+\frac{1}{2},k} - \frac{U_{i+\frac{1}{2},k}U_{i+\frac{1}{2},k} + V_{i+\frac{1}{2},k}V_{i+\frac{1}{2},k}}{2}}, \tag{59}$$

where $\varepsilon_{i,k} = [E_{i,k} + P_{i,k}]/\rho_{i,k}$.

$\bar{H}^n_{i,k+\frac{1}{2}}$ is a numerical estimate of the flux through the top interface of cell i,k evaluated at time level n. It may be calculated using equations (47) through (59) with $i+1,k$ replaced by $i,k+1$, $i+\frac{1}{2},k$ replaced by $i,k+\frac{1}{2}$, $\hat{\Omega}_x$ equal to $Y_{i-\frac{1}{2},k+\frac{1}{2}} - Y_{i+\frac{1}{2},k+\frac{1}{2}}$, ($\eta_x/J$ evaluated at $i,k+\frac{1}{2}$) and $\hat{\Omega}_y$ equal to $X_{i+\frac{1}{2},k+\frac{1}{2}} - X_{i-\frac{1}{2},k+\frac{1}{2}}$ (η_y/J evaluated at $i,k+\frac{1}{2}$).

After Chakravarthy [2], the value of $1/J$ at the centre of each cell is taken to be the area of the cell. Thus the value of $1/J$ in the centre of cell j,k is given by

$$\begin{aligned}\frac{1}{J_{i,k}} &= \frac{1}{2}\left[X_{i-\frac{1}{2},k-\frac{1}{2}} - X_{i+\frac{1}{2},k+\frac{1}{2}}\right]\left[Y_{i+\frac{1}{2},k-\frac{1}{2}} - Y_{i-\frac{1}{2},k+\frac{1}{2}}\right] \\ &+ \frac{1}{2}\left[X_{i+\frac{1}{2},k-\frac{1}{2}} - X_{i-\frac{1}{2},k+\frac{1}{2}}\right]\left[Y_{i+\frac{1}{2},k+\frac{1}{2}} - Y_{i-\frac{1}{2},k-\frac{1}{2}}\right].\end{aligned} \tag{60}$$

Note that it is the components of $\bar{U}$ that are conserved. That is, the average of each component of $\underline{U}$ times the area of the cell is conserved. The flux through an interface between two adjacent cells increases the value of $\bar{U}$ in one cell by the same amount by which it decreases the value of $\underline{U}$ in the adjacent cell. However, if the area of the adjacent cells is different, then the values of the change in $\underline{U}$ in each cell will not be of equal size. Degradation of the solution will not occur if the cell sizes and shapes vary smoothly across the physical domain. That is, the most accurate numerical solutions are obtained when $1/J$ varies smoothly across the domain.

The explicit time-step size is either held constant or is set equal to the maximum allowed explicit time-step size (based on the maximum allowed Courant number) decreased by a problem-dependent multiplicative factor. The Courant number for cell i,k is taken to be the sum, over the four sides of the cell, of $\frac{|\lambda^{max}|}{2}\beta_{i,k}$.

The grid may consist of several rectangular subgrids. Reflection or transmission boundary conditions may be specified at the left, right, bottom or top edge of a subgrid. Two additional boundary conditions may be specified at the left and right edge of a subgrid: supersonic inflow and continuation of the solution from an adjacent subgrid. It is convenient, in what follows, to discuss the implementation of boundary conditions at the left edge of a grid. The discussion is easily generalized to describe boundary conditions at the right, bottom, or top edge of a grid.

A reflection boundary condition is implemented by adding two columns of virtual cells (designated outer- and inner-column) to the left of the boundary. The values of the components of $\underline{U}$ in the virtual cells are assigned so that E, ρ, and parallel gas velocity are symmetric about the boundary while the gas velocity perpendicular to the boundary is antisymmetric. Since the Euler equations are inviscid, slippage is allowed along walls. In other words, it is assumed that the flow near the boundary approximates that which would occur if a stream of gas meets a parallel flowing stream in such a way that no matter crosses the boundary. Two rows of virtual cells are required to compute the interface flux at the boundary because of the method of construction of the flux-limiters. As a seldom used option, the compression parameter may be set to zero when computing the interface flux at a reflective boundary so that the data in the outer column of virtual cells does not effect the solution.

Transmission boundary conditions were initially also implemented by simply adding two columns of virtual cells to the left of the boundary. The value of $\underline{U}$ in the virtual cells was assigned so that $\underline{U}$ would be symmetric about the boundary. This simple scheme resulted in unsatisfactory transmission of rarefaction waves in a one-dimensional Euler problem solved using the TVD scheme. It was soon determined that rarefaction waves were transmitted without extraneous reflections if the first-order upwind method was employed instead. A great deal of further numerical experimentation showed that much smaller extraneous reflections could be obtained for the TVD scheme if the compression parameter was set to zero when computing the interface flux at the boundary and at the interface just to the right of the boundary. The zero values of compression parameter at the two interfaces caused the value of the solution in the (real) cell just to the right of the boundary to be, in effect, computed using the first-order upwind method. The extraneous reflections were due to an unwitting attempt to use higher-order accuracy at a boundary and are related to the difficulties experienced by Kamowitz [8] when using greater than zero-order extrapolation of flow velocities for a transmission boundary condition.

An alternative approach to transmission boundary conditions has been developed by extending the characteristic extrapolation scheme of Kamowitz for use in two-dimensional domains. The alternative approach gives equivalent quality in one-dimensional problems and reduces extraneous reflections in two-dimensional problems. An extra column of image cells is used along the left edge of the domain to store boundary data. (An extra column or row of image cells is placed along the right, top, and bottom edge of the domain to deal with transmissive left, upper, and lower boundaries.) The data in the column of image cells is used instead of an inner column of virtual cells. Before the TVD scheme is applied the value of $\underline{U}_{0,k}$ for the image cells are updated using

$$\underline{U}^{n+1}_{0,k} = \underline{U}^{n}_{0,k} - \beta_{1,k}\left[\frac{\underline{f}(\underline{U}^{n}_{1,k}) - \underline{f}(\underline{U}^{n}_{0,k})}{2}\hat{\Omega}_x + \frac{\underline{h}(\underline{U}^{n}_{1,k}) - \underline{h}(\underline{U}^{n}_{0,k})}{2}\hat{\Omega}_y\right], \qquad (61)$$

where $\hat{\Omega}_x = Y_{\frac{1}{2},k+\frac{1}{2}} - Y_{\frac{1}{2},k-\frac{1}{2}}$ and $\hat{\Omega}_y = X_{\frac{1}{2},k-\frac{1}{2}} - X_{\frac{1}{2},k+\frac{1}{2}}$ incorporate the effect of the length

and orientation of the boundary interface on the row-wise flux into cell 0,k. It is convenient to evaluate $\beta = J\Delta t$ at the center of (real) cell $1,k$ rather than (image) cell $0,k$. The procedure amounts to application of characteristic extrapolation in the row-wise direction. Best results are produced when the solution in the outer column of virtual cells is set to the updated solution in the column of image cells.

Characteristic extrapolation is also performed at the right edge of the domain if there is a transmission boundary there. The TVD scheme is then applied to the entire grid including image columns but the row-wise TVD fluxes are set to zero when computing the TVD flux into an image-column cell owing to the prior addition of the row-wise flux using characteristic extrapolation.

A similar procedure is used to apply transmission boundary conditions at the top and bottom of the domain. Since the TVD fluxes are computed one cell-column at a time, it is convenient compute the row-wise TVD fluxes within a cell-column, then apply column-wise characteristic extrapolation to update the solution in an image cell at the top or bottom of the cell-column, finally followed by computation of column-wise TVD fluxes within the cell-column. Column-wise TVD fluxes are set to zero when computing the TVD flux into an image cell at the top or bottom of the cell-column, owing to the prior addition of the column-wise flux using characteristic extrapolation.

Note that a cell which is at the intersection of a row and column of image cells is only updated using characteristic extrapolation. The difference in the order of application of TVD fluxes and of characteristic extrapolation in the row-wise and column-wise directions does not result in detectable degradation of the solution.

Cell-columns are updated from left to right within a subgrid. Continuation boundary conditions are handled automatically as long as the solution in a subgrid is not computed until the solution in all the subgrids to its left have been computed. A supersonic inflow left-boundary condition is handled by leaving two columns of cells at the left side of the domain whose values are never updated but are simply used to compute row-wise fluxes into the left boundary.

The TVD time-stepping is applied one cell-column at a time by calling a highly vectorized subroutine. The subroutine is supplied with the old values of the solution at the centers and the spatial coordinates at the corners of the cells in the column that is to be updated (designated column b). The old values of the solution within the cell-column to the left (column a) and within the two cell-columns to the right of column b (columns c and d) are also supplied. Cell columns a, b, c, or d may be given virtual values to aid in specifying reflection or transmission left or right boundary conditions. Two extra cells are appended to the top and bottom of all four cell columns and may be given virtual values to aid in the specification of transmission or reflection upper or lower boundary conditions. The values of row-wise interface flux into the left-hand sides of the cells in column b form part of the input into the subroutine. The subroutine returns the updated values of the solution within cell-column b along with the values of row-wise flux out of the right-hand sides of the cells.

The flux limiter 'minmod' was used exclusively during the early stages of code development. As discussed by Yee [3], there are a number of alternative flux limiters that have been used by various authors. The very compressive limiter of Roe, 'superbee', as modified by Sweby [9], was introduced in the later stages of code development. This limiter

results in particularly thin contact surfaces. The function 'superbee(a,b)' is the maximum of 'minmod(a,ωb)' and 'minmod(ωa,b)'.

Expressions of the form $\frac{1}{2}[1\pm\theta]$minmod$(a,\omega b)+\frac{1}{2}[1\mp\theta]$minmod$(\omega a,b)$ in equation (49) are replaced by superbee(a,b) to yield

$$W^m_{i+\frac{1}{2},k} = \frac{|\lambda^m_{i+\frac{1}{2},k}|}{2}\alpha^m_{i+\frac{1}{2},k} + \frac{\lambda^{m-}_{i+\frac{1}{2},k}}{2}\text{superbee}(\alpha'^m_{i+\frac{3}{2},k},\alpha^m_{i+\frac{1}{2},k}) - \frac{\lambda^{m+}_{i+\frac{1}{2},k}}{2}\text{superbee}(\alpha^m_{i+\frac{1}{2},k},\alpha'^m_{i-\frac{1}{2},k}). \quad (62)$$

The altered expressions are larger near transitions and hence cancel out a greater portion of the first term in $W^m_{i+\frac{1}{2},k}$. For a given value of ω, the differencing has a smaller first-order upwind component when 'superbee' is used instead of 'minmod'. The maximum Courant number must not exceed $2/[2+\omega]$, and ω must not exceed 2. As recommended in Yee [3] and Sweby [9], 'superbee' is only employed in computing the second and third weights (associated with characteristic velocity U_c) in the sum of equation (47). If 'superbee' is used to compute the first and fourth weights (associated with characteristic velocities $U_c \mp C$), oscillations occur in smooth regions for large Mach numbers.

6.0 RESULTS OF EXPLICIT TVD CALCULATIONS

The TVD code was initially developed on a Perkin Elmer 3250 at UTIAS. The initial installation of the TVD code on the Cray X-MP/24 at the Ontario Centre for Large Scale Computation resulted in a 100-fold increase in execution speed. Subsequent tailoring of the code to allow increased vectorization and more efficient output yielded an additional increase in execution speed by a factor of four.

It is of interest to discuss a one-dimensional problem solved on a 200-cell grid. Figure 1 illustrates density profiles at various times for a planar shock tube initially having three regions with zero gas velocity and the same temperature but with the central region having one-tenth of the pressure of the outer regions. The three regions are separated by two bursting diaphragms. Shock waves proceed into the low-pressure region and reflect at the centre of the shock tube. Rarefaction waves propagate into the high-pressure regions and reflect off the closed ends of the shock tube. Contact surfaces between the gas cooled by a rarefaction wave and the gas heated by a shock wave move with the flow towards the centre.

Use of flux limiters to reduce the calculation to first order near steep transitions has prevented development of the oscillations near shocks typical of conventional second-order accurate calculations. The compression parameter of 'minmod' was set to 1 and that of 'superbee' was set to 1.25. Slightly larger values of the compression parameters resulted in shocks that were not flat at the top. Somewhat larger values of the compression parameters could be used if the initial pressure ratio across the diaphragms was reduced to two. The value of θ was set to $\frac{1}{2}$ since that gave the thinnest transitions. The above computation will be designated calculation ST1 (Shock Tube 1) in what follows.

If the compression parameters are set to zero, then the first-order upwind method is obtained. The profiles in figure 2 were generated by a first-order upwind calculation and display much broader density transitions than are seen in figure 1, especially for the contact surface.

It will have been noticed that there are small moving bumps in the reflecting rarefaction waves in figure 1. The bumps quickly disappear after the rarefaction waves have been

completely reflected. The bumps do not appear if smaller compression parameters are used, but the transitions become thicker. The small fixed bumps that remain attached to each end of the shock tube do not disturb the rest of the flow field and may not be present depending on how the reflection boundary condition is enforced. The bumps do not appear if the initial pressure ratio across the bursting diaphragms is reduced to two.

The TVD code was used to solve a two-dimensional test problem on a four-unit by four-unit square domain on which a three-unit by three-unit centrally located square region initially had one-tenth the density of the surrounding region. This was the so-called 'shock-box' problem of Aki. The gas flow over one-quarter of the domain was modelled on a 200-cell by 200-cell grid with perpendicular reflection boundary conditions imposed on the bottom and right-hand sides of the grid and transmission boundary conditions imposed on the other two sides.

Figures 3a and 3b illustrate the resulting lines of constant density at times $t = 0.375$ and $t = 0.5625$ if only the limiter 'minmod', with $\theta = \frac{1}{2}$, is used. A shock wave proceeds inwards, trailed by a contact surface, and a rarefaction wave moves outwards. The two legs of the rarefaction wave reflect at the corner to produce a very steep rarefaction. The entire computation required about 5 CPU minutes and will be designated calculation SQR1 in what follows.

The compression parameter had to be set to 0.75 to suppress oscillations where the two legs of the rarefaction wave reflected. This adjustment resulted in thickening of the shock wave and contact surface. Note that reduction of the compression parameter to a value between zero and one is equivalent to maintaining a first-order upwind component of difference, over the entire flow field.

Figure 4 illustrates the resulting lines of constant density at $t = 0.5625$ if 'superbee' is used for m equal to two and three in a computation that will be designated as calculation SQR2. The compression parameter of 'minmod' is set to 0.75 and that of 'superbee' is set to 1.25. The shock wave is slightly thinner and the contact surface is considerably reduced in thickness. There are a few small wiggles visible. Use of smaller compression parameters will suppress the wiggles but result in thicker transitions. It is clear that use of a TVD code involves selection of priorities that depend on the use to which the solution will be applied. Use of 'superbee' increases the execution time to about 6 minutes because of a reduction in the permitted Courant number. If 'minmod' is retained but with a compression parameter of 1.25 for m equal to two and three, the execution time, thickness of the transitions, and abundance wiggles are intermediate between that of calculation SQR1 and that of calculation SQR2.

The accuracy of the code was tested by computing the flows resulting from a planar shock with a Mach number of 3.72 incident from the right on a 40-degree wedge. The compression parameter of 'minmod' was set to 0.75 and that of 'superbee' was set to 1.25 and θ was set to one. The calculation required about 27 CPU minutes.

The 500-cell by 110-cell grid grid and contours of constant density obtained by calculation 'WEDGE1' are illustrated in figure 5. The upper surface of the wedge lies along the bottom edge of the grid. Hence, perpendicular reflection boundary conditions were imposed at the bottom edge. Transmission boundary conditions were imposed on the other three edges of the grid. The leftmost contour lines consist of a Mach stem (moving perpendicular to the surface of the wedge) and the remaining portion of the (vertical) incident shock that meet the reflected shock at a sharp angle. The reflected shock consists of a straight contour

joined to a curved contour at a point of inflection. A second Mach stem is attached at the point of inflection and extends towards the wedge surface. A slip stream is seen to extend from the top of the first Mach stem to near the base of the second Mach stem. All the flow structures are very well resolved, and the contours of constant density are a good match to contours computed by Glaz, Colella, Glass, and Deschambault [12] using experimental data.

Calculation 'WEDGE2', in which the compression parameter for 'minmod' is increased to one, develops supersonic flow near the surface of the wedge that deforms the base of the leading Mach stem as shown in figure 6. The amount of deformation increases with the strength of the incident shock and the size of compression parameter or time-step. Because the deformation decreases as the compression parameters are increased, it is conjectured that the deformation is a consequence of the absence of viscosity in a region that is experiencing large pressure changes due to shock reflection but which would be inside a boundary layer if the full Navier-Stokes equations were being solved. Similar behaviour has occurred for θ equal to $\frac{1}{2}$, zero, or minus one.

The code has been tested on its ability to solve problems on multiply-connected domains having curved boundaries. Supersonic flow resulting from the impingement from the right of a shock with a Mach number of 6 on an inlet of more or less arbitrary shape has been modelled using a 388-cell by 80-cell grid.

The grid and contours of constant density are illustrated in figure 7. Planar geometry is assumed; hence, the non-gridded regions with curved outlines at the bottom and interior of the grid represent a cowl and underbody of uniform cross section in the direction perpendicular to the plane of the figure. The width of the cell columns was varied so that the cell height would be approximately equal to the cell width within the inlet. Transmission boundary conditions were imposed on the left, right, and top sides of the grid. Perpendicular reflection boundary conditions are imposed at the surfaces of the cowl and underbody. The domain was broken into four subgrids, with continuation boundary conditions imposed at the interfaces. The compression parameters for 'minmod' and 'superbee' were both set to one, and θ was set to $\frac{1}{2}$. This calculation took about 36 CPU minutes.

In figure 7b, the solution has approached a near-steady state flow. The small horizontal gap in the contouring occurs because the contours on the top 40 and bottom 40 rows of cells are computed separately and are based on density values at the centres of the cells. A bow shock remains attached to the leading edge of the underbody. A second shock remains detached from the leading edge of the cowl but merges with the bow shock to reinforce it. The incident shock passes through the inlet and the left-hand boundary, leaving shocks attached to the trailing edges of the inlet. The flow through the inlet undergoes compression and expansion as it proceeds towards the trailing shocks. The flow over the top of the cowl encounters a rarefaction wave attached to the cowl's trailing edge.

The code has been tested in its ability to solve flows through the inlet models placed in the hypersonic impulse tunnel located at UTIAS. Figure 8 illustrates the 476-cell by 40-cell grid used to to compute the upper half of the flow field for a Prandtl-Meyer inlet and the resulting contours of constant density at $t = 1.2$, $t = 4.2$, and $t = 4.8$. The widths of the cells decrease from left to right in a linear manner. The leading edge of the inlet is four cell-columns from the left-hand side of the grid. Reflection boundary conditions are imposed along the walls of the inlet and along the bottom of the grid. Transmission boundary conditions are imposed on all other edges of the grid. The area ratio of the inlet

was about 9.1 to one. The compression parameters for 'minmod' and 'superbee' were set to one and 1.15, respectively, and θ was set to $\frac{1}{2}$. Calculation 'PM1' took about 46 CPU minutes.

At the start of the calculation the first two cell-columns in the grid contain gas flowing to the right at a Mach number of 8.4 towards the inlet in which the gas is stationary. The ratios of the temperature and density of the gas in the first two cell-columns to temperature and density of the gas in the rest of the domain are $\frac{2}{7}$ and seventy, respectively. The ratios of the gasdynamical variables are losely based on some one-dimensional predictions of conditions in the test section of the impulse tunnel that were performed by Groth [13]. As illustrated in figure 8b, this initial discontinuity in the flow variables separates into a rightward moving shock wave trailed by a contact surface and an upstream-facing rarefaction wave.

The region in the vicinity of the throat of the Prandtl-Meyer inlet has been enlarged by a factor of five in figure 8d to display the time-asymptotic contours of constant density. The flow encounters a compression fan produced by the curved wall of the leading portion of the inlet and eventually reaches a region of increased constant pressure adjacent to a portion of wall that is straight. The compression characteristics coalesce into a shock which is reflected off the centre of symmetry along the bottom of the grid and strikes the wall of the inlet just downstream of the corner where the walls of the inlet become horizontal. The gas near the wall in the region of increased constant pressure encounters the corner before reaching the reflected shock and produces a rarefaction fan which crosses the reflected shock to produce an expansion in the throat of the inlet.

The Courant number increased by a factor of three during one time-step. This did not lead to visible deterioration of the solution because the size of the next time-step was reduced by a factor of three to satisfy the limitation on Courant number. However, a more sophisticated time-step strategy, still based on the size of Courant number but allowing repetition of a time-step under certain conditions, would increase the reliability of the calculation.

It is desirable to use as large an initial density ratio as is possible to match experimental conditions for which the inlet is initially at vacuum pressures. The trailing contact surface and rarefaction wave in the numerical solution decrease in strength and eventually cease to be present as the density ratio is increased. Variant density ratios result in the same steady state solution since the rarefaction wave and contact surface are eventually swept out of the domain but small density ratios do result in less realistic unsteady flows. Unfortunately, if a density ratio of 140 is used in the numerical calculations the solution only proceeds to $t = 2.4$ before negative densities occur, presumably, because of a sudden increase in Courant number.

7.0 IMPLICIT SOLUTION OF TVD EQUATIONS

An implicit predictor-corrector method has been developed that is first-order accurate in time and requires the storage of $\dot{\underline{U}}$ (the first-order time-derivatives of $\underline{U}$) for each cell. The time derivatives at time-level n, $\dot{\underline{U}}^n_{i,k}$, are used in the predictor equation

$$\underline{U}^{n+1(0)}_{i,k} = \underline{U}^n_{i,k} + \Delta t \dot{\underline{U}}^n_{i,k}\,, \tag{63}$$

to extrapolate the solution at time-level n to obtain $\underline{U}^{n+1(0)}_{i,k}$, an initial approximation to the solution at time-level $n+1$. Newton's method with simplifications is applied to a modified

form of equation (46) to obtain a corrector equation. Development of the corrector equation is described in detail below.

The interface flux, $\bar{F}^n_{i+\frac{1}{2},k}$, may be be written in the alternative forms

$$\bar{F}^n_{i+\frac{1}{2},k} = \frac{\underline{f}(\underline{U}^n_{i+1,k}) - \underline{f}(\underline{U}^n_{i,k})}{2}\hat{\Omega}_x + \frac{\underline{h}(\underline{U}^n_{i+1,k}) - \underline{h}(\underline{U}^n_{i,k})}{2}\hat{\Omega}_y - \sum_{m=1}^{4} W^m_{i+\frac{1}{2},k}\underline{R}^m_{i+\frac{1}{2},k}$$
$$+\underline{f}(\underline{U}^n_{i,k})[Y_{i+\frac{1}{2},k+\frac{1}{2}} - Y_{i+\frac{1}{2},k-\frac{1}{2}}] + \underline{h}(\underline{U}^n_{i,k})[X_{i+\frac{1}{2},k-\frac{1}{2}} - X_{i+\frac{1}{2},k+\frac{1}{2}}]. \quad (64)$$

and

$$\bar{F}^n_{i+\frac{1}{2},k} = -\frac{\underline{f}(\underline{U}^n_{i+1,k}) - \underline{f}(\underline{U}^n_{i,k})}{2}\hat{\Omega}_x - \frac{\underline{h}(\underline{U}^n_{i+1,k}) - \underline{h}(\underline{U}^n_{i,k})}{2}\hat{\Omega}_y - \sum_{m=1}^{4} W^m_{i+\frac{1}{2},k}\underline{R}^m_{i+\frac{1}{2},k}$$
$$+\underline{f}(\underline{U}^n_{i+1,k})[Y_{i+\frac{1}{2},k+\frac{1}{2}} - Y_{i+\frac{1}{2},k-\frac{1}{2}}] + \underline{h}(\underline{U}^n_{i+1,k})[X_{i+\frac{1}{2},k-\frac{1}{2}} - X_{i+\frac{1}{2},k+\frac{1}{2}}]. \quad (65)$$

If $\beta_{i,k}[\bar{F}^n_{i+\frac{1}{2},k} - \bar{F}^n_{i-\frac{1}{2},k}]$ is evaluted using equations (64) and (65) the second lines in these equations give rise to the expression $\beta_{i,k}\underline{f}(\underline{U}^n_{i,k})\tilde{Y}_{\eta\xi} - \beta_{i,k}\underline{h}(\underline{U}^n_{i,k})\tilde{X}_{\eta\xi}$ where $\tilde{Y}_{\eta\xi}$ and $\tilde{X}_{\eta\xi}$ are approximations to $Y_{\eta\xi}$ and $X_{\eta\xi}$ evaluated using central differences in cell i,k. In a similar manner, if $\beta_{i,k}[\bar{H}^n_{i,k+\frac{1}{2}} - \bar{H}^n_{i,k-\frac{1}{2}}]$ is evaluated using equations analogous to equations (64) and (65), the expression $-\beta_{i,k}\underline{f}(\underline{U}^n_{i,k})\tilde{Y}_{\xi\eta} + \beta_{i,k}\underline{h}(\underline{U}^n_{i,k})\tilde{X}_{\xi\eta}$ is obtained. The two expressions cancel because the differencing method has been chosen so that $\tilde{Y}_{\xi\eta} = \tilde{Y}_{\eta\xi}$ and $\tilde{X}_{\xi\eta} = \tilde{X}_{\eta\xi}$. Thus, for cell i,k, all terms proportional to $\underline{f}(\underline{U}^n_{i,k})$ and $\underline{h}(\underline{U}^n_{i,k})$ within the expressions for the interface fluxes $\bar{F}^n_{i+\frac{1}{2},k}$, $\bar{F}^n_{i-\frac{1}{2},k}$, $\bar{H}^n_{i,k+\frac{1}{2}}$, and $\bar{H}^n_{i,k-\frac{1}{2}}$ may be made to cancel. As a consequence, the right-hand side of equation (46) can be reformulated in terms of differences of $\underline{f}$, $\underline{h}$, and $\underline{U}$ across cell interfaces.

If the differences in $\underline{f}$ and $\underline{h}$ are linearized in terms of the differences in $\underline{U}$, equation (46) without the source term may be approximated by

$$\underline{U}^{n+1}_{i,k} - \underline{U}^n_{i,k} = -\beta_{i,k}\sum_{m=1}^{4}\lambda^{m-}_{i+\frac{1}{2},k}\alpha^m_{i+\frac{1}{2},k}\underline{R}^m_{i+\frac{1}{2},k} + \lambda^{m+}_{i-\frac{1}{2},k}\alpha^m_{i-\frac{1}{2},k}\underline{R}^m_{i-\frac{1}{2},k}$$
$$-\beta_{i,k}\sum_{m=1}^{4}\lambda^{m-}_{i,k+\frac{1}{2}}\alpha^m_{i,k+\frac{1}{2}}\underline{R}^m_{i,k+\frac{1}{2}} + \lambda^{m+}_{i,k-\frac{1}{2}}\alpha^m_{i,k-\frac{1}{2}}\underline{R}^m_{i,k-\frac{1}{2}}$$
$$-\beta_{i,k}\sum_{m=1}^{4}\Phi^m_{i+\frac{1}{2},k}\underline{R}^m_{i+\frac{1}{2},k} - \Phi^m_{i-\frac{1}{2},k}\underline{R}^m_{i-\frac{1}{2},k}$$
$$-\beta_{i,k}\sum_{m=1}^{4}\Phi^m_{i,k+\frac{1}{2}}\underline{R}^m_{i,k+\frac{1}{2}} - \Phi^m_{i,k-\frac{1}{2}}\underline{R}^m_{i,k-\frac{1}{2}}, \quad (66)$$

where $\Phi^m_{i+\frac{1}{2},k}$ is simply $-W^m_{i+\frac{1}{2},k}$ with the first term removed because of its incorporation in $\lambda^{m-}_{i+\frac{1}{2},k}$ used in the first row of equation (66). The quantities $\underline{R}^m_{i,k+\frac{1}{2}}$, $\alpha^m_{i,k+\frac{1}{2}}$, and $\Phi^m_{i,k+\frac{1}{2}}$ are computed at the upper interface of cell i,k using formulae analogous to those used for the right-hand interface. The relationship between equation (46) and equation (66) is similar to the relationship between equation (25) and equation (2) using the interface flux of equation (28).

Equation (66) has the disadvantage that it is not in conservative-difference form but has the advantage that it is simple to linearize for implicit calculations. The right-hand side of equation (66) is essentially a linear function of the cell-interface differences in $\underline{U}$ that are contained within the factors $\alpha^m_{i\pm\frac{1}{2},k}$ and $\alpha^m_{i,k\pm\frac{1}{2}}$; the quantities $\lambda^m_{i\pm\frac{1}{2},k}$, $\underline{L}^m_{i\pm\frac{1}{2},k}$, $\underline{R}^m_{i\pm\frac{1}{2},k}$, $\lambda^m_{i,k\pm\frac{1}{2}}$, $\underline{L}^m_{i,k\pm\frac{1}{2}}$, and $\underline{R}^m_{i,k\pm\frac{1}{2}}$ are relatively slowly changing functions of the components of $\underline{U}$.

Chakravarthy [2] has derived the corrector equation

$$
\begin{aligned}
&-[A^+]_{i-\frac{1}{2},k}\delta\underline{U}^{n+1(Q)}_{i-1,k} + \left(\frac{[I]}{2\beta_{i,k}} + [A^+]_{i-\frac{1}{2},k} - [A^-]_{i+\frac{1}{2},k}\right)\delta\underline{U}^{n+1(Q)}_{i,k} + [A^-]_{i+\frac{1}{2},k}\delta\underline{U}^{n+1(Q)}_{i+1,k} \\
&-[A^+]_{i,k-\frac{1}{2}}\delta\underline{U}^{n+1(Q)}_{i,k-1} + \left(\frac{[I]}{2\beta_{i,k}} + [A^+]_{i,k-\frac{1}{2}} - [A^-]_{i,k+\frac{1}{2}}\right)\delta\underline{U}^{n+1(Q)}_{i,k} + [A^-]_{i,k+\frac{1}{2}}\delta\underline{U}^{n+1(Q)}_{i,k+1} \\
&\qquad = -\frac{1}{\beta_{i,k}}\left[\underline{U}^{n+1(Q-1)}_{i,k} - \underline{U}^{n}_{i,k}\right] - \bar{S}^{n+1(Q-1)}_{i,k} \\
&\qquad - \left[\bar{F}^{n+1(Q-1)}_{i+\frac{1}{2},k} - \bar{F}^{n+1(Q-1)}_{i-\frac{1}{2},k}\right] - \left[\bar{H}^{n+1(Q-1)}_{i,k+\frac{1}{2}} - \bar{H}^{n+1(Q-1)}_{i,k-\frac{1}{2}}\right],
\end{aligned}
\tag{67}
$$

where $[I]$ is a 4×4 identity matrix, $[A^\pm]_{i,k\mp\frac{1}{2}}$ is a 4×4 matrix giving the influence of a difference in components of $\underline{U}$ across interface $i, k\mp\frac{1}{2}$ on the value of components of $\underline{U}_{i,k}$, $\underline{U}^{n+1(Q)}_{i,k}$ is the result of the Q^{th} correction of the solution, $\bar{F}^{n+1(Q-1)}_{i+\frac{1}{2},k}$ and $\bar{H}^{n+1(Q-1)}_{i,k+\frac{1}{2}}$ are interface fluxes computed using the previous estimate of the solution, and $\delta\underline{U}^{n+1(Q)}_{i,k} = \underline{U}^{n+1(Q)}_{i,k} - \underline{U}^{n+1(Q-1)}_{i,k}$ is the residual of the solution (departure from the previous estimate of the solution) in each cell. The left-hand side of equation(67) may be obtained by applying Newton's method to equation (66) with the last two lines discarded so as to retain only first-order accuracy and by treating the first two lines as linear functions of the cell-interface differences in $\underline{U}$. The right-hand side of equation (67) uses the right-hand side of equation (46) so as to obtain the advantages of the conservative-difference form. Equation (67) for all i, k is assembled into a sparse matrix system which may be solved for all $\delta\underline{U}^{n+1(Q)}_{i,k}$.

The influence matrix, $[A^\pm]_{i,k\mp\frac{1}{2}}$, is computed using

$$
[A^\pm]_{i,k\mp\frac{1}{2}} = \sum_{m=1}^{4} \underline{R}^m_{i,k\mp\frac{1}{2}}\lambda^{m\pm}_{i,k\mp\frac{1}{2}}\underline{L}^m_{i,k\mp\frac{1}{2}} = [R]_{i,k\mp\frac{1}{2}}[\lambda^\pm]_{i,k\mp\frac{1}{2}}[L]_{i,k\mp\frac{1}{2}}, \tag{68}
$$

where $[\lambda^\pm]_{i,k\mp\frac{1}{2}}$ is a diagonal matrix whose diagonal elements are $\lambda^{m\pm}_{i,k\mp\frac{1}{2}}$. It is usually convenient to evaluate $[A^\pm]_{i,k\mp\frac{1}{2}}$ in terms of the previous estimate of the solution, $\underline{U}^{n+1(Q-1)}$, in the appropriate cells. The matrix $[A^\pm]_{i\mp\frac{1}{2},k}$ is computed in an analogous manner.

An early version of the implicit algorithm which was developed for simplified problems in which one spatial dimension was suppressed by using only one column of cells and computing column-wise fluxes only, will now be described. Time-step control was closely modelled after that of the predictor-corrector method of Gear [14]. The predictor equation is the same as given above. The corrector consists of a block-tridiagonal equation with rows given by

$$
\begin{aligned}
&-[A^+]_{i,k-\frac{1}{2}}\delta\underline{U}^{n+1(Q)}_{i,k-1} + \left(\frac{[I]}{\beta_{i,k}} + [A^+]_{i,k-\frac{1}{2}} - [A^-]_{i,k+\frac{1}{2}}\right)\delta\underline{U}^{n+1(Q)}_{i,k} + [A^-]_{i,k+\frac{1}{2}}\delta\underline{U}^{n+1(Q)}_{i,k+1} \\
&\qquad = -\frac{1}{\beta_{i,k}}\left[\underline{U}^{n+1(Q-1)}_{i,k} - \underline{U}^{n}_{i,k}\right] - \left[\bar{H}^{n+1(Q-1)}_{i,k+\frac{1}{2}} - \bar{H}^{n+1(Q-1)}_{i,k-\frac{1}{2}}\right] - \bar{S}^{n+1(Q-1)}_{i,k},
\end{aligned}
\tag{69}
$$

obtained by suppressing the terms with indices $i \pm \frac{1}{2}, k$ in equation (67).

The residuals of density and total energy per unit volume are used to compute the quantity

$$\frac{3}{2N}\sum_{k=1}^{N}\left|\frac{E_{i,k}^{n+1(Q)}-E_{i,k}^{n+1(Q-1)}}{E_{i,k}^{n}}\right|+\left|\frac{\rho_{i,k}^{n+1(Q)}-\rho_{i,k}^{n+1(Q-1)}}{\rho_{i,k}^{n}}\right|, \tag{70}$$

which is compared to a specified tolerance (denoted *TOL* in what follows) as a test for convergence after each application of the corrector. The time-step size is quartered if *TOL* is still exceeded after a specified number of corrections (usually 3) are performed. The accumulated residuals constitute the 'correction' to the solution at each cell.

If the convergence test is passed within the specified number of applications of the corrector, the corrections to E and ρ are used to compute the error estimate,

$$EST=\frac{1}{4N}\sum_{k=1}^{N}\left|\frac{E_{i,k}^{n+1(Q)}-E_{i,k}^{n+1(0)}}{E_{i,k}^{n}}\right|+\left|\frac{\rho_{i,k}^{n+1(Q)}-\rho_{i,k}^{n+1(0)}}{\rho_{i,k}^{n}}\right|. \tag{71}$$

The step fails if *EST* is larger than *TOL*. Regardless of success or failure of the error test, the maximum allowed size of time-step is estimated by multiplying the current size of time-step by the ratio

$$\frac{1}{1.2\left[\sqrt{\frac{EST}{TOL}}+10^{-6}\right]}, \tag{72}$$

but the size of time-step is only allowed to increase on every second time-step if the ratio has exceeded 1.2 on the last ten time-steps.

On the event of a successful step the corrections are also used to update stored values of $\Delta t\dot{\underline{U}}$ for each cell. If the convergence or error tests are not passed, the step is retried with the indicated reduction of time-step size. The values of $\Delta t\dot{\underline{U}}$ are adjusted for changes in the size of time-step. The explicit algorithm is used to compute the values of $\Delta t\dot{\underline{U}}$ at the start of execution of the code and whenever the error test has failed three times in a row.

It was soon determined that larger time-steps could be achieved if certain off-diagonal coefficients of $[A^{\pm}]_{i,k\mp\frac{1}{2}}$ were set to zero so as to make the matrix equation more diagonally dominant. In a later development, inspired by the work of Yee [3], $[\lambda^{\pm}]_{i,k\mp\frac{1}{2}}$ was replaced by a diagonal matrix whose diagonals were all equal to $\lambda_{i,k\mp\frac{1}{2}}^{max\pm}$ where $\lambda_{i,k\mp\frac{1}{2}}^{max}$ was chosen to be the value of λ^m at interface $i, k \mp \frac{1}{2}$ with maximum magnitude. Despite the use of the less accurate influence matrices time-step size was typically doubled because diagonal dominance was enhanced. The execution time devoted to computation of matrix coefficients was greatly reduced because $[A^{\pm}]_{i,k\mp\frac{1}{2}}$ was simplified to $\lambda_{i,k\mp\frac{1}{2}}^{max\pm}[I]$. The execution time devoted to matrix inversion was also greatly reduced because the block-tridiagonal system was replaced by four tridiagonal systems, one for each component of $\underline{U}$.

The implicit time-stepping strategy, described above, exhibits an excellent ability to predict optimum time-step size and demonstrates a robust recovery from failure of corrector-convergence or error-size tests when applied to a number of one-dimensional problems. Owing to the fact that the left-hand side of equation (69) is only of first-order accuracy, shock waves and contact surfaces tend to be thicker for the implicit method than for the explicit method if the same values of compression parameters are used. Increasing the size

of the compression parameters for implicit calculations reduces the increase in thickness and gives more satisfactory results in some cases.

Time-step size control based on the magnitude of *EST* gives good results for one-dimensional problems but is inconvenient to use in two dimensional problems because of the necessity of storing the corrections to $\underline{U}$ over the entire domain. The strategy that has been developed for two-dimensional problems is to set the implicit time-step size to the maximum allowed explicit time-step size enlarged by a problem-dependent multiplicative factor.

Direct solution of equation (67) involves the inversion of a matrix that can have a very large bandwidth. After Chakravarthy [2] the off-diagonal terms in the row-wise direction are discarded. The equations are further simplified by use of $\lambda^{max\pm}$ in the influence matrices. The resultant tridiagonal-matrix equation, with rows given by

$$-\lambda^{max+}_{i,k-\frac{1}{2}}\delta\underline{U}^{n+1(Q)}_{i,k-1} + \left(\frac{1}{\beta_{i,k}} + \lambda^{max+}_{i,k-\frac{1}{2}} - \lambda^{max-}_{i,k+\frac{1}{2}}\right)\delta\underline{U}^{n+1(Q)}_{i,k} + \lambda^{max-}_{i,k+\frac{1}{2}}\delta\underline{U}^{n+1(Q)}_{i,k+1}$$
$$+\left(\lambda^{max+}_{i-\frac{1}{2},k} - \lambda^{max-}_{i+\frac{1}{2},k}\right)\delta\underline{U}^{n+1(Q)}_{i,k} = -\frac{1}{\beta_{i,k}}\left[\underline{U}^{n+1(Q-1)}_{i,k} - \underline{U}^{n}_{i,k}\right] - \bar{S}^{n+1(Q-1)}_{i,k}$$
$$-\left[\bar{F}^{n+1(Q-1)}_{i+\frac{1}{2},k} - \bar{F}^{n+1(Q-1)}_{i-\frac{1}{2},k}\right] - \left[\bar{H}^{n+1(Q-1)}_{i,k+\frac{1}{2}} - \bar{H}^{n+1(Q-1)}_{i,k-\frac{1}{2}}\right], \qquad (73)$$

is solved cell-column by cell-column to provide quick relaxation of the residuals along the column-wise direction. Note that the coefficients of $\delta\underline{U}^{n+1(Q)}_{i,k}$ are all positive and exceed the sum of the coefficients of the off-diagonal residuals so that the system of equations is diagonally dominant. The tridiagonal matrices associated with each of the components of $\underline{U}$ are identical if reflection or transmission boundary conditions at the top or bottom of the cell-column are handled appropriately. Relaxation of the residuals along the row-wise direction is induced by application of the corrector in left to right sweeps across the domain as described below.

At the start of each time-step the solution over the entire domain is predicted using equation (63). The tridiagonal corrector equation is then applied once within each cell-column in a preliminary sweep through the entire domain. On subsequent sweeps the corrector is only applied within cell-columns that are adjacent to a continuation boundary, that failed the convergence test on a previous sweep, or that are within a margin of eight columns of a cell-column which failed the convergence test. Sweeping is discontinued when all cell-columns have passed the convergence test. The number of sweeps required is typically less than ten.

Attempts to allow use of more than one application of the corrector in each cell-column during a sweep increase the number of sweeps to more than 25 before all cell-columns pass the convergence test on the first application of the corrector. Use of only one application of the corrector in each cell-column gives a more nearly equal propagation of information in the column-wise and row-wise directions.

8.0 RESULTS OF IMPLICIT TVD CALCULATIONS

The thickness of a moving shock-wave is doubled if calculation PM1 is repeated with implicit time-stepping; despite this, the implicit and explicit calculations converge to the same steady-state solution. A larger initial density ratio may be used than in the explicit calculations. Figure 9 displays contours of constant density at $t = 1.2$ and $t = 4.2$, obtained

by repeating calculation PM1 with an initial density ratio of 140 and with the compression parameters for 'minmod' and 'superbee' set to one and 1.25, respectively. As shown in figure 9a, the strengths of the trailing contact surface and rarefaction wave are considerably reduced. Execution time was only increased by fifteen per cent because multiple application of the corrector was only required in the vicinity of the moving waves and because the specified limit on size of Courant number was 43 per cent larger than in the explicit calculation.

Figure 10 illustrates the 500-cell by 48-cell grid for a spike inlet with the same area ratio as was used for the Prandtl-Meyer inlet. The bottom of the grid conforms to the shape of the cylindrically symmetrical spike whose point is located four cell-columns from the left-hand side of the grid. There is a narrow slit in the right-hand side of the grid to accomadate a cowl. Reflection boundary condition are imposed along the bottom of the grid and on the surface of the cowl. Transmission boundary conditions are imposed on all other edges of the grid. The domain is broken up into three subgrids, with continuation boundary conditions imposed at the interfaces. The widths of the cells decrease from left to right in a linear manner and linear stretching of the cell heights was applied in the upper 24 rows of cells. The same initial ratios of gasdynamical variables were used as in calculation PM1. The compression parameters for 'minmod' and 'superbee' were set to 0.75 and one, respectively, and θ was set to one. The implicit calculation took about 88 CPU minutes.

Contours of constant density at $t = 1.2$ and at $t = 4.8$ and contours of constant pressure in the vicinity of the cowl with five times the resolution at $t = 4.8$ are shown in figure 11. Gas flowing at a Mach number of 8.4 approaches the inlet from the left and is compressed by the spike before entry into the annular space between the spike and cowl. The flow encounters a compression fan produced by the curved surface of the spike and eventually reaches a region of increased constant pressure near the (conical) base of the spike. The point of focus of the compression fan is not clearly illustrated in figure 11c because the pressure contours in the top 24 and bottom 24 cell-rows are computed separately, leaving a gap in the contour lines. However, the fact that there are only two contour lines over the top of the cowl indicates that there is little spillage of the flow. The compression fan reflects off the underside of the leading edge of the cowl as a shock. The shock crosses the expansion fan produced by flow about the corner at the base of the spike and is reflected back towards the cowl at a position downstream of the corner. The separate structures of the expansion fan and shock wave downstream of their point of intersection were not resolved in a plot of the contours of constant density.

Attempts to use a larger initial density ratio have failed thus far owing to the evolution of negative densities. If explicit time-stepping is employed, the solution only proceeds to $t = 2.4$ before the calculation fails owing to the evolution of negative densities.

9.0 TVD EXPLICIT MACCORMACK BASED METHOD

An alternate form of explicit TVD code, based on the work of Yee [3], has been developed in which the method of MacCormack is applied as the first half of a time-step. The two-stage MacCormack algorithm may be expressed as

$$\breve{\underline{U}}^n_{i,k} = \underline{U}^n_{i,k} - \beta_{i,k}\Delta\bar{F}(\underline{U}^n)_{i-\frac{1}{2},k} - \beta_{i,k}\Delta\bar{H}(\underline{U}^n)_{i,k+\frac{1}{2}} - \beta_{i,k}\bar{S}(\underline{U}^n)_{i,k} \tag{74}$$

followed by

$$\tilde{\underline{U}}^{n+1}_{i,k} = \underline{U}^n_{i,k} + \frac{1}{2}\left[\breve{\underline{U}}^n_{i,k} - \underline{U}^n_{i,k} - \beta_{i,k}\Delta\bar{F}(\breve{\underline{U}}^n)_{i+\frac{1}{2},k} - \beta_{i,k}\Delta\bar{H}(\breve{\underline{U}}^n)_{i,k-\frac{1}{2}}\right] - \beta_{i,k}\bar{S}(\breve{\underline{U}}^n)_{i,k}\,. \tag{75}$$

Here

$$\Delta\bar{H}(\breve{\underline{U}}^n)_{i,k-\frac{1}{2}} = \left[\underline{f}(\breve{\underline{U}}^n_{i,k}) - \underline{f}(\breve{\underline{U}}^n_{i,k-1})\right]\hat{\Omega}_x + \left[\underline{h}(\breve{\underline{U}}^n_{i,k}) - \underline{h}(\breve{\underline{U}}^n_{i,k-1})\right]\hat{\Omega}_y \tag{76}$$

is the flux difference across interface $i, k-\frac{1}{2}$ where $\hat{\Omega}_x$ and $\hat{\Omega}_y$ are η_x/J and η_y/J, respectively, evaluated at interface $i, k-\frac{1}{2}$. The flux-differences $\Delta\bar{F}(\breve{\underline{U}}^n)_{i+\frac{1}{2},k}$, $\Delta\bar{H}(\underline{U}^n)_{i,k+\frac{1}{2}}$, and $\Delta\bar{F}(\underline{U}^n)_{i-\frac{1}{2},k}$ are computed using similar formulae. The resulting solution is spatially and temporally of second-order accuracy if the grid is uniform. The MacCormack equations can be applied cell-column by cell-column from left to right across the domain in one sweep if $\breve{\underline{U}}^n_{i,k-1}$, the value of the intermediate solution in cell $i, k-1$ in the previous cell-column, is retained for use in computing the second-stage fluxes into cell i, k.

The post-processor

$$\begin{aligned}\underline{U}^{n+1}_{i,k} = \tilde{\underline{U}}^n_{i,k} &- \beta_{i,k}\sum_{m=1}^{4}\tilde{\Phi}^m_{i+\frac{1}{2},k}\tilde{\underline{R}}^m_{i+\frac{1}{2},k} - \tilde{\Phi}^m_{i-\frac{1}{2},k}\tilde{\underline{R}}^m_{i-\frac{1}{2},k} \\ &- \beta_{i,k}\sum_{m=1}^{4}\tilde{\Phi}^m_{i,k+\frac{1}{2}}\tilde{\underline{R}}^m_{i,k+\frac{1}{2}} - \tilde{\Phi}^m_{i,k-\frac{1}{2}}\tilde{\underline{R}}^m_{i,k-\frac{1}{2}}\,,\end{aligned} \tag{77}$$

is then applied to obtain a TVD solution. Here

$$\tilde{\Phi}^m_{i+\frac{1}{2},k} = \frac{|\tilde{\lambda}^m_{i+\frac{1}{2},k}| - \beta_{i+\frac{1}{2},k}(\tilde{\lambda}^m_{i+\frac{1}{2},k})^2}{2}\left[\tilde{Q}^m_{i+\frac{1}{2},k} - \tilde{\alpha}^m_{i+\frac{1}{2},k}\right], \tag{78}$$

where $\beta_{i+\frac{1}{2},k} = [\beta_{i+1,k} + \beta_{i,k}]/2$ and $\tilde{Q}^m_{i+\frac{1}{2},k}$ is a limiter term which for m equal to 1 or 4 is given by

$$\begin{aligned}\tilde{Q}^m_{i+\frac{1}{2},k} &= -\tilde{\sigma}^{m-}_{i+\frac{1}{2},k}\left(\frac{1-\theta}{4}\text{minmod}(\tilde{\alpha}'^m_{i+\frac{3}{2},k}, \omega\tilde{\alpha}^m_{i+\frac{1}{2},k}) + \frac{1+\theta}{4}\text{minmod}(\omega\tilde{\alpha}'^m_{i+\frac{3}{2},k}, \tilde{\alpha}^m_{i+\frac{1}{2},k})\right) \\ &+ \tilde{\sigma}^{m+}_{i+\frac{1}{2},k}\left(\frac{1+\theta}{4}\text{minmod}(\tilde{\alpha}^m_{i+\frac{1}{2},k}, \omega\tilde{\alpha}'^m_{i-\frac{1}{2},k}) + \frac{1-\theta}{4}\text{minmod}(\omega\tilde{\alpha}^m_{i+\frac{1}{2},k}, \tilde{\alpha}'^m_{i-\frac{1}{2},k})\right)\end{aligned} \tag{79}$$

and for m equal to 2 or 3 is given by

$$\tilde{Q}^m_{i+\frac{1}{2},k} = -\frac{\tilde{\sigma}^{m-}_{i+\frac{1}{2},k}}{2}\text{superbee}(\tilde{\alpha}'^m_{i+\frac{3}{2},k}, \tilde{\alpha}^m_{i+\frac{1}{2},k}) + \frac{\tilde{\sigma}^{m+}_{i+\frac{1}{2},k}}{2}\text{superbee}(\tilde{\alpha}^m_{i+\frac{1}{2},k}, \tilde{\alpha}'^m_{i-\frac{1}{2},k}). \tag{80}$$

Note that the quantity $\beta_{i+\frac{1}{2},k}(\tilde{\lambda}^m_{i+\frac{1}{2},k})^2$ is computed before the sonic correction is applied to $\tilde{\lambda}^m_{i+\frac{1}{2},k}$ since the post-processor must replace the Lax-Wendroff-like interface-flux of the MacCormack method with first-order upwind differences in regions of rapid change in the solution. $\tilde{\Phi}^m_{i,k+\frac{1}{2}}$ is calculated in a similar manner.

Owing to the action of the post-processor, there is little need to alternate between backward and forward flux differences in equations (74) and (75) from time-step to time-step as would be required if the MacCormack method was used by itself. However, such alternation is left as an option in the code for the column-wise flux differences, $\Delta\bar{H}_{i,k\pm\frac{1}{2}}$.

10.0 RESULTS OF EXPLICIT TVD-MACCORMACK CALCULATIONS

Figure 12 illustrates the results of repeating calculation STR1 with identical parameters but using the TVD-MacCormack scheme. The density transitions are slightly thicker and there is a small bump at the top of the shocks. Note the absence of bumps in the reflected rarefaction wave. The positions of the various wave fronts corresponds to those obtained in calculation ST1 but there is a small difference in some of the wave forms.

Calculation SQ2 was repeated using the TVD-MacCormack scheme. As shown in figure 13, the density transitions resulting from calculation SQR3 are only slightly thicker than those from calculation SQR2. Execution time was increased by about 14 per cent, despite the use of an identical number of time-steps, because of the two-stage nature of the MacCormack scheme.

Calculation WEDGE1 has also been repeated using the TVD-MacCormack scheme. As shown in figure 14 there is a reasonable correspondence in the contours of constant density except near the base of the leading Mach stem where deformation is evident. Execution time was increased by about 26 per cent because of the two-stage nature of the MacCormack scheme and because of a slight increase in the number of time-steps. Experimentation with the sizes of the compression parameters or time-step would reduce the deformation but not the execution time.

Figure 15 illustrates the 424-cell by 40-cell grid and the contours of constant density at $t = 1.2$ and $t = 4.2$, for the Prandtl-Meyer inlet obtained by using the TVD-MacCormack scheme with the compression parameters for 'minmod' and 'superbee' both set one and with θ set to $\frac{1}{2}$. The contours of constant density at $t = 4.2$ obtained by calculation PM3 are in reasonable agreement with those obtained by calculation PM1 even though a different grid was used. At $t = 1.2$ the trailing rarefaction wave and contact surface are weaker than in calculation PM1 (the same strength as in calculation PM2) because it was possible to use a density ratio of 140 without encountering numerical difficulties.

11.0 CONCLUSIONS

The quality of the calculations is sensitive to the time-step size, the method of flux limiting, and the value of compression parameter. Nonetheless, with a little attention to selection of parameters, it is currently possible to obtain excellent results with the TVD code on domains of complex configuration using explicit time-stepping. Some improvement could be made in the strategy for selection of size of time-step based on Courant number.

Owing to the use of selective solution predictor-corrector procedures, the execution times for inviscid two-dimensional problems using implicit time-stepping are only slightly greater than the execution times required for explicit time-steps. Both implicit and explicit time-stepping converge to the same steady-state solution. The relative efficiency of implicit time-stepping would be much greater for viscid flows. In some cases an implicit calculation will run to completion for conditions that cause the failure of an explicit calculation.

The TVD-MacCormack code requires greater execution times than the originally implemented explicit method and has not yet given better quality solutions in most cases. It may prove to have increased value if converted to use implicit time-stepping.

As it stands now, the TVD code in its various versions forms an excellent basis for extension to the solution of viscid flows through domains of complex configuration using the real gas-equation of state. Extension to the use of three-dimensional domains is straightforward although computationally expensive.

References

[1] P. L. Roe, *Approximate Riemann solvers, parameter vectors, and difference schemes*, Journal of Computational Physics **43**, pp. 357–372, 1981.

[2] S. R. Chakravarthy, *Development of upwind schemes for the Euler equations*, NASA CR–4043, 1987.

[3] H. C. Yee, *Upwind and symmetric shock-capturing schemes*, NASA TM–89464, 1987.

[4] D. A. Anderson, J. C. Tannehill, R. H. Pletcher, *Computational fluid mechanics and heat transfer*, McGraw-Hill, New York, 1984.

[5] R. W. MacCormack, *The effect of viscosity in hypervelocity impact cratering*, AIAA Paper 69-354, 1969.

[6] P. D. Lax, B. Wendroff, *Systems of conservation laws*, Communications of Pure and Applied Mathematics, **13**, pp. 217–237, 1960.

[7] A. Harten, J. M. Hyman, P. D. Lax, *On finite-difference approximations and entropy conditions for shocks*, Communications of Pure and Applied Mathematics **29**, pp. 297–322, 1976.

[8] D. Kamowitz, *Some Observations on Boundary Conditions for Numerical Conservation Laws*, ICASE Report 88-67, 1988.

[9] P. K. Sweby, *High resolution schemes using flux limiters for hyperbolic conservation laws*, SIAM Journal on Numerical Analysis **21**(5), pp. 995–1011, 1984.

[10] P. L. Roe, J. Pike, *Efficient construction and utilization of approximate Riemann solutions*, *in* Computing Methods in Applied Sciences and Engineering VI, R. Glowinsky, J. L. Lions (editors), North-Holland, 1984.

[11] P. D. Thomas, C. K. Lombard, *Geometric conservation law and its application to flow computations on moving grids*, AIAA Journal **17**(10), pp. 1030–1037, 1979.

[12] H. M. Glaz, P. Colella, I. I. Glass, R. L. Deschambault, *A detailed numerical, graphical, and experimental study of oblique shock wave reflections*, University of Toronto Institute for Aerospace Studies Report 285, 1986.

[13] C. P. T. Groth, *Private communication*, 1989.

[14] C. W. Gear, *Numerical initial value problems in ordinary differential equations*, Prentice Hall, New Jersey, 1971.

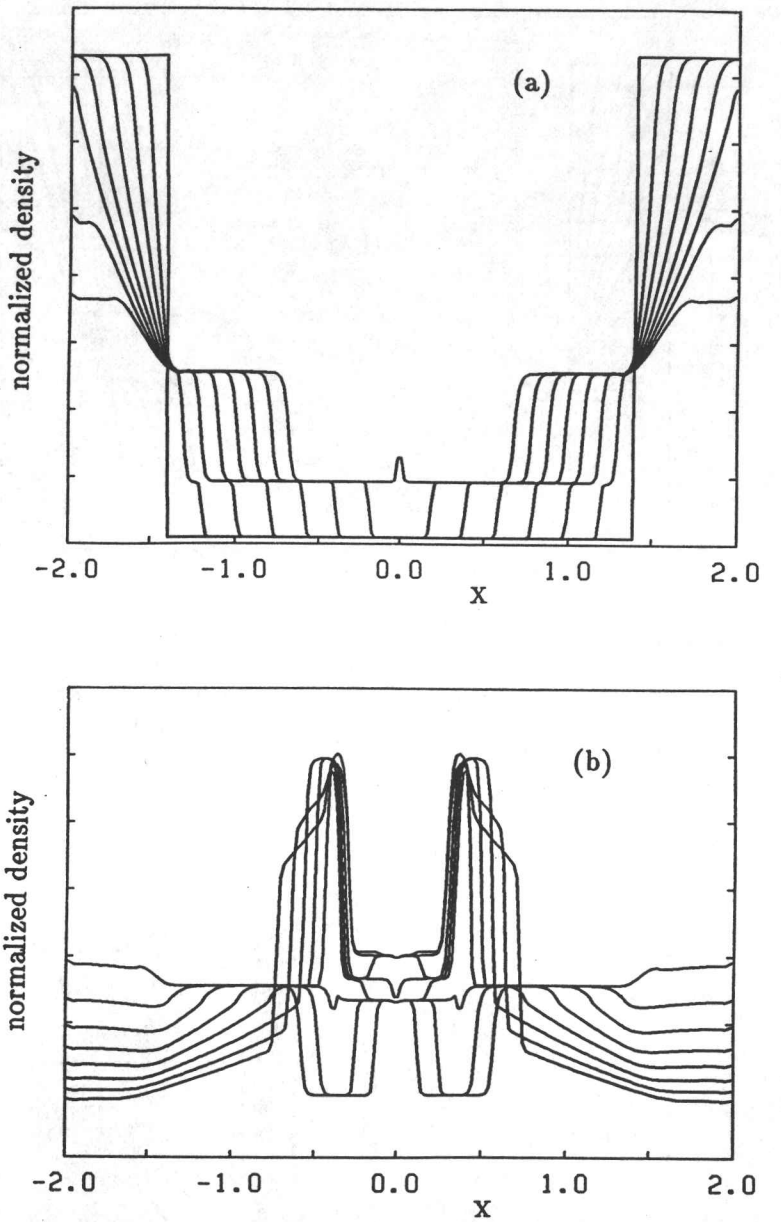

Fig. 1 ST1: Density profiles from $t = 0$ to $t = 0.875$ (a) and from $t = 1$ to $t = 1.875$ (b) for a one-dimensional shock-tube problem, obtained with 'minmod' and 'superbee' compression parameters set to 1 and 1.25, respectively. Approximate time intervals between profiles is $\Delta t = 0.125$. Calculations were performed on a 200-cell grid.

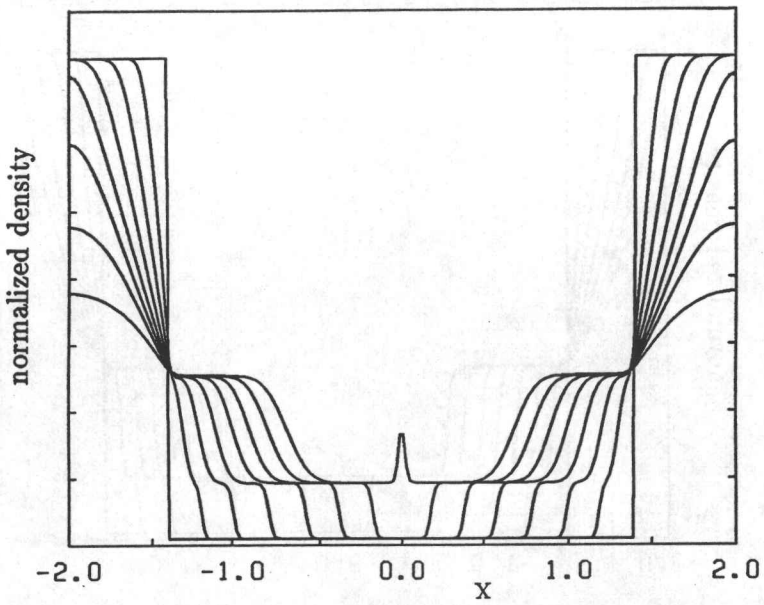

Fig. 2 Density profiles from $t = 0$ to $t = 0.875$ for the one-dimensional shock-tube problem, obtained with 'minmod' and 'superbee' compression parameters both set to zero. Approximate time interval between profiles is $\Delta t = 0.125$. Calculations were done on a 200-cell grid.

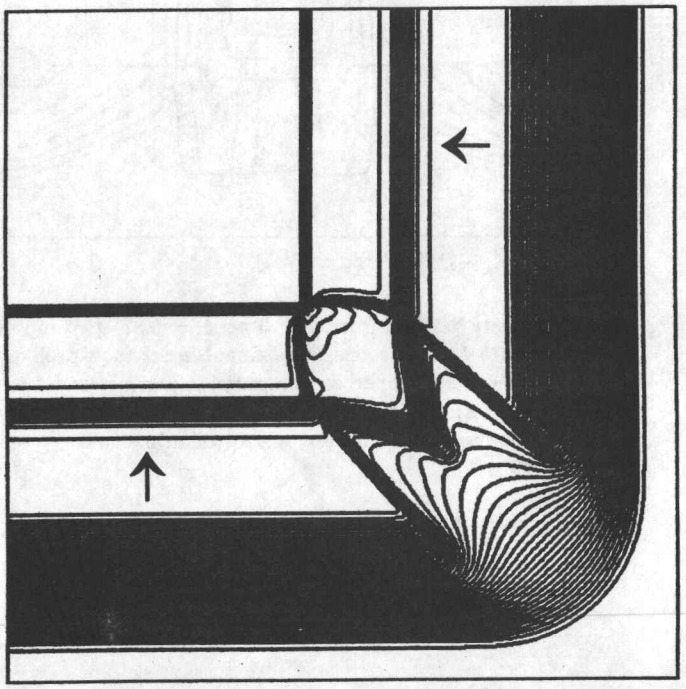

Fig. 3a SQR1: Contours of constant density for the 'shock-box' problem at $t = 0.375$, obtained with the 'minmod' compression parameter set to 0.75. Computations were done with a 200-cell by 200-cell grid.

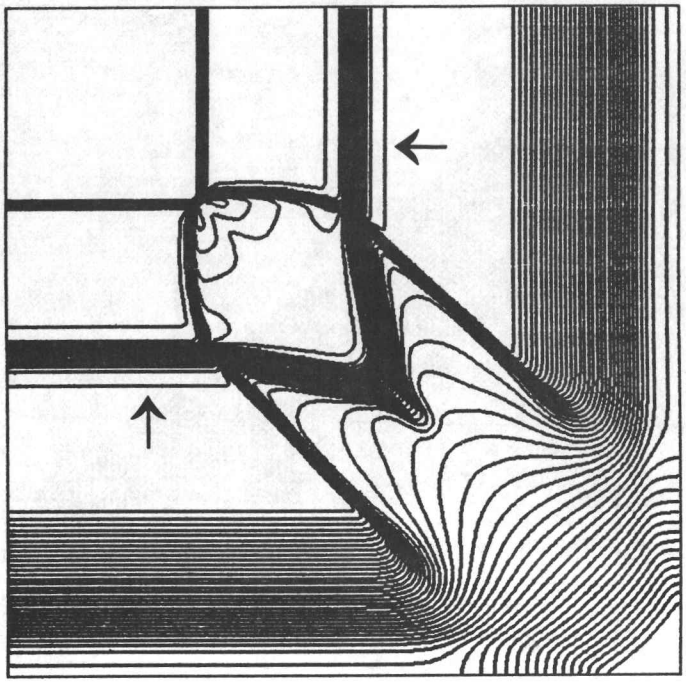

Fig. 3b SQR1: Contours of constant density for the 'shock-box' problem at $t = 0.5625$, just after the rarefaction wave has reflected off the solid walls of the box, obtained with a 'minmod' compression parameter set to 0.75.

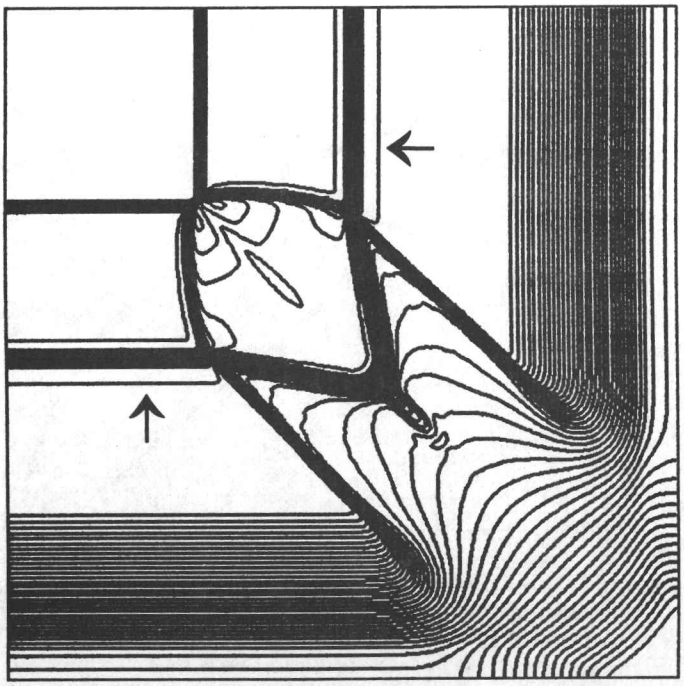

Fig. 4 SQR2: Contours of constant density for the 'shock-box' problem at $t = 0.5625$, just after the rarefaction wave has reflected off the solid walls of the box, obtained with 'minmod' and 'superbee' compression parameters set to 0.75 and 1.25, respectively. Computations were done with a 200-cell by 200-cell grid.

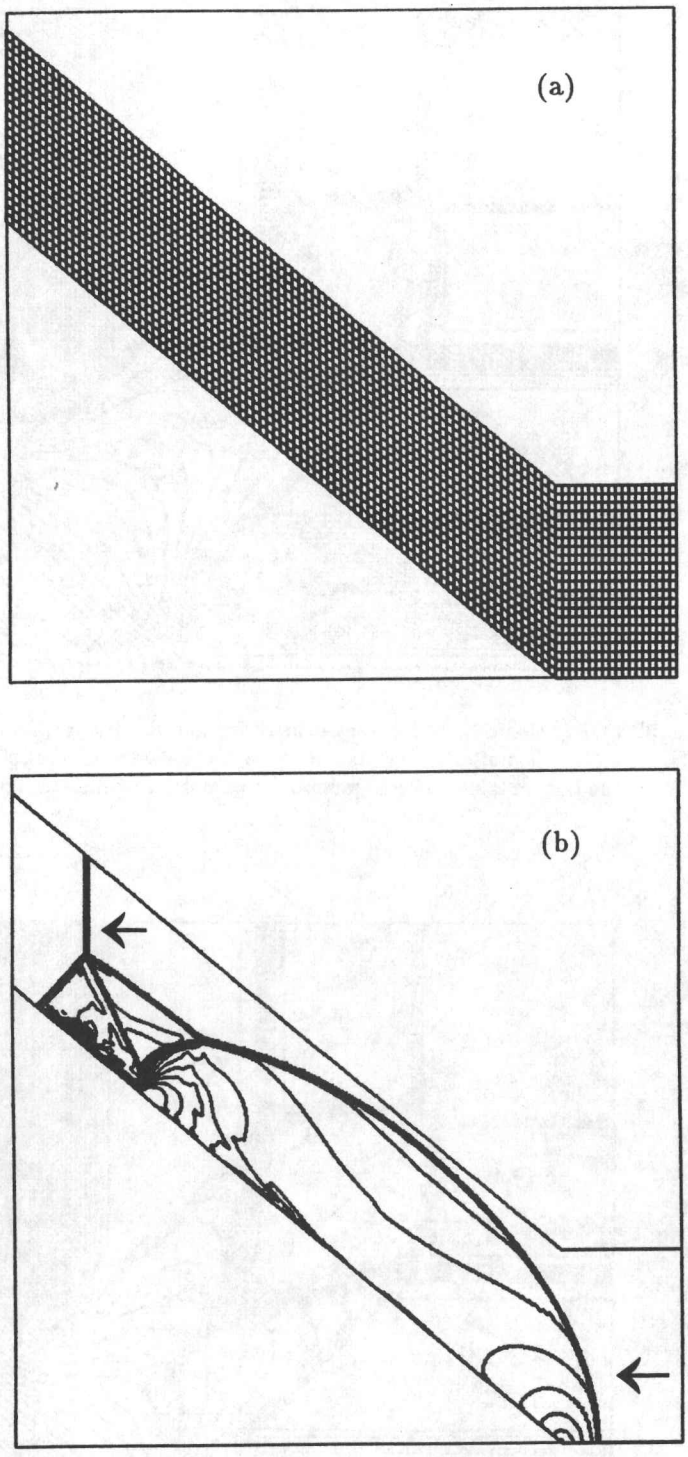

Fig. 5 WEDGE1: Grid for Mach-3.72 shock incident from the right on a 40 degree wedge (a), and contours of constant density (b), obtained with 'minmod' and 'superbee' compression parameters set to 0.75 and 1.25, respectively. Only every fifth grid line is shown to maintain clarity.

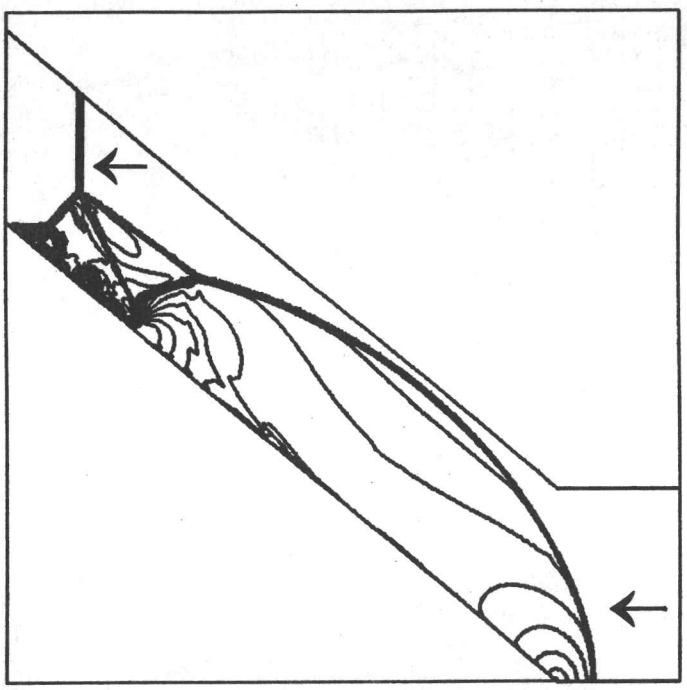

Fig. 6 WEDGE2: Contours of constant density for Mach-3.72 shock incident from the right on the wedge, obtained with 'minmod' compression parameter increased to 1.0.

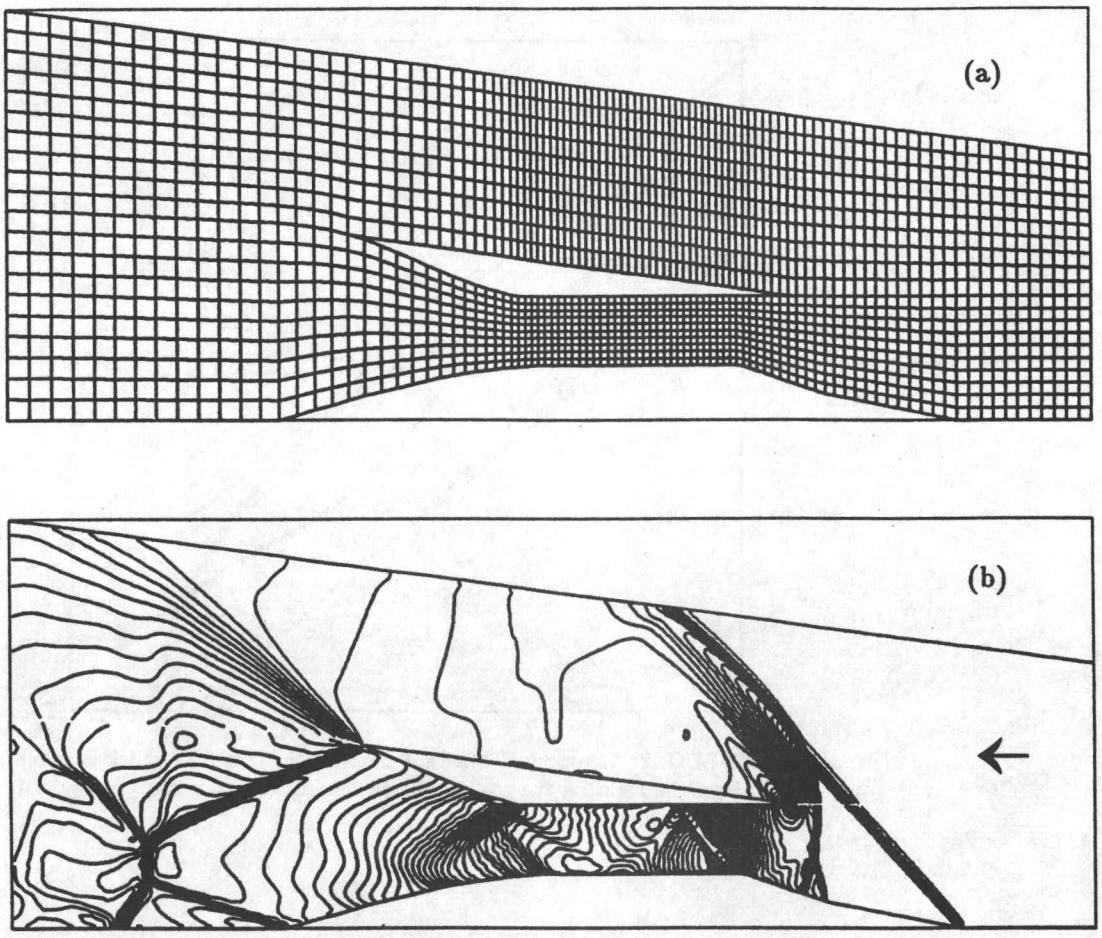

Fig. 7 Grid for Mach-6 shock incident from the right on an inlet (a), and contours of constant density (b), obtained with 'minmod' and 'superbee' compression parameters both set one. Only every fourth grid line is shown.

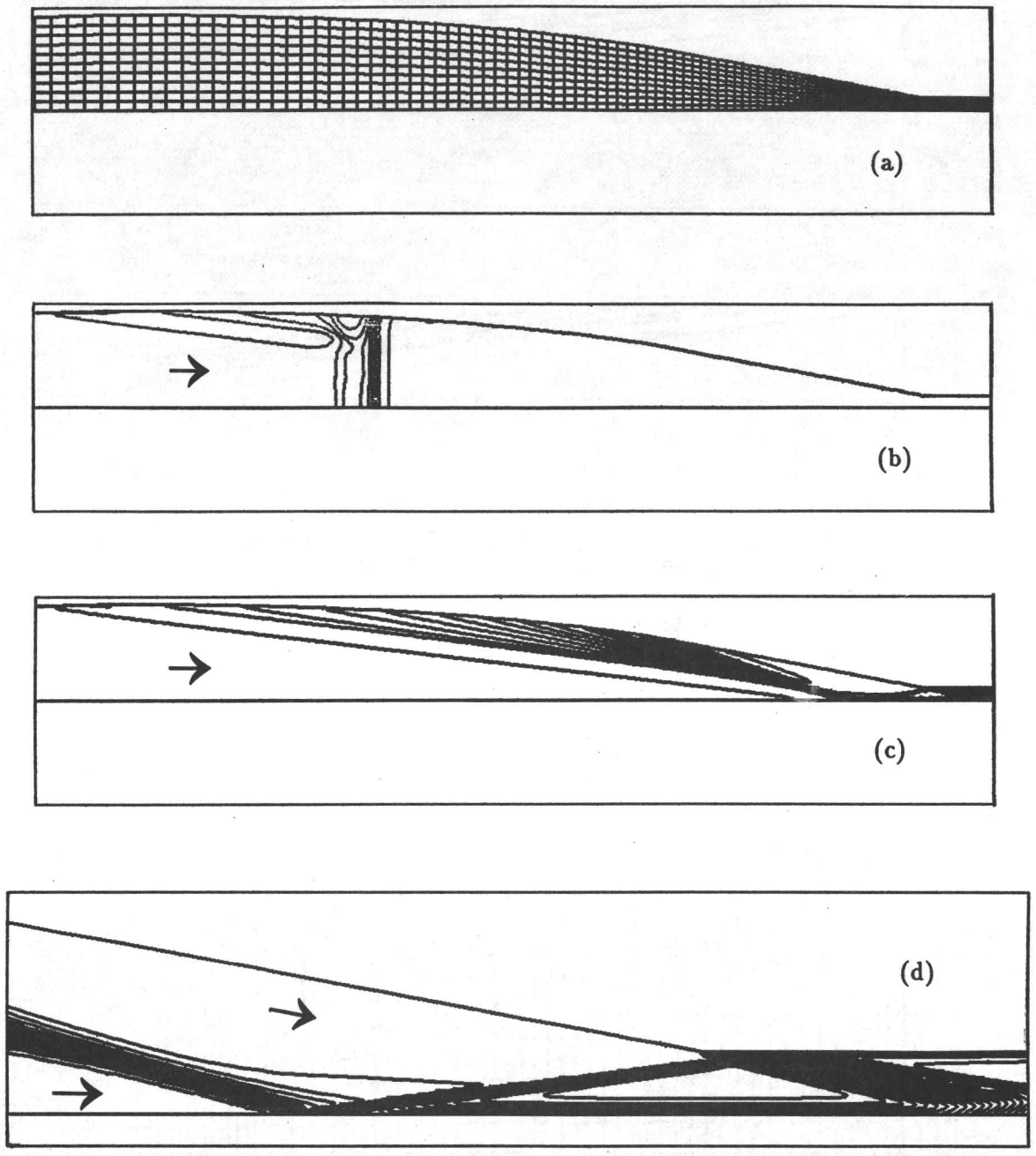

Fig. 8 PM1: Grid for Mach-8.4 flow from the right into a Prandtl-Meyer inlet (a), and contours of constant density at $t = 1.2$ (b), at $t = 4.2$ (c), and at $t = 4.8$ with increased resolution (d), obtained with 'minmod' and 'superbee' compression parameters set to 1.0 and 1.15, respectively. Only every fourth grid line is shown.

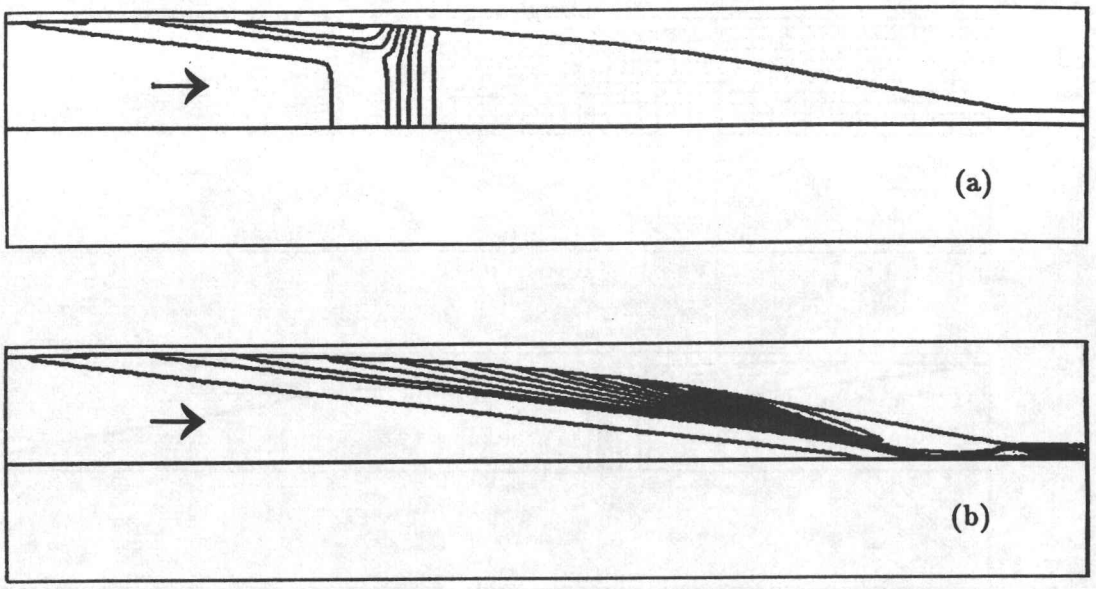

Fig. 9 PM2: Contours of constant density for Mach-8.4 flow from right into the Prandtl-Meyer inlet at $t = 1.2$ (a) and at $t = 4.2$ (b), obtained using implicit time-stepping with 'minmod' and 'superbee' compression parameters set to 1.0 and 1.15, respectively.

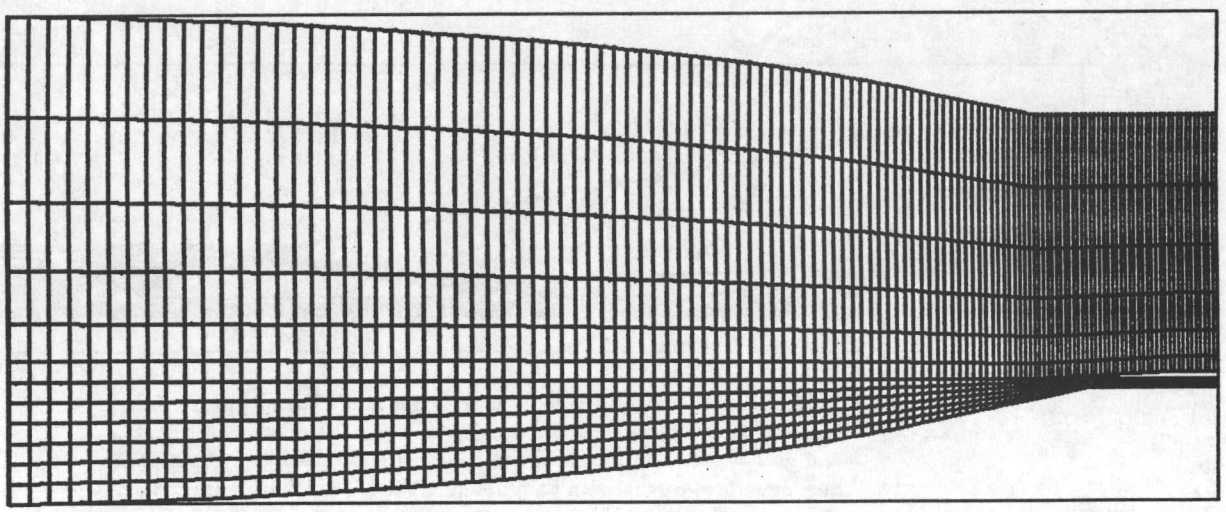

Fig. 10 Grid for Mach-8.4 flow from right into a spike inlet. Only every fourth grid line is shown.

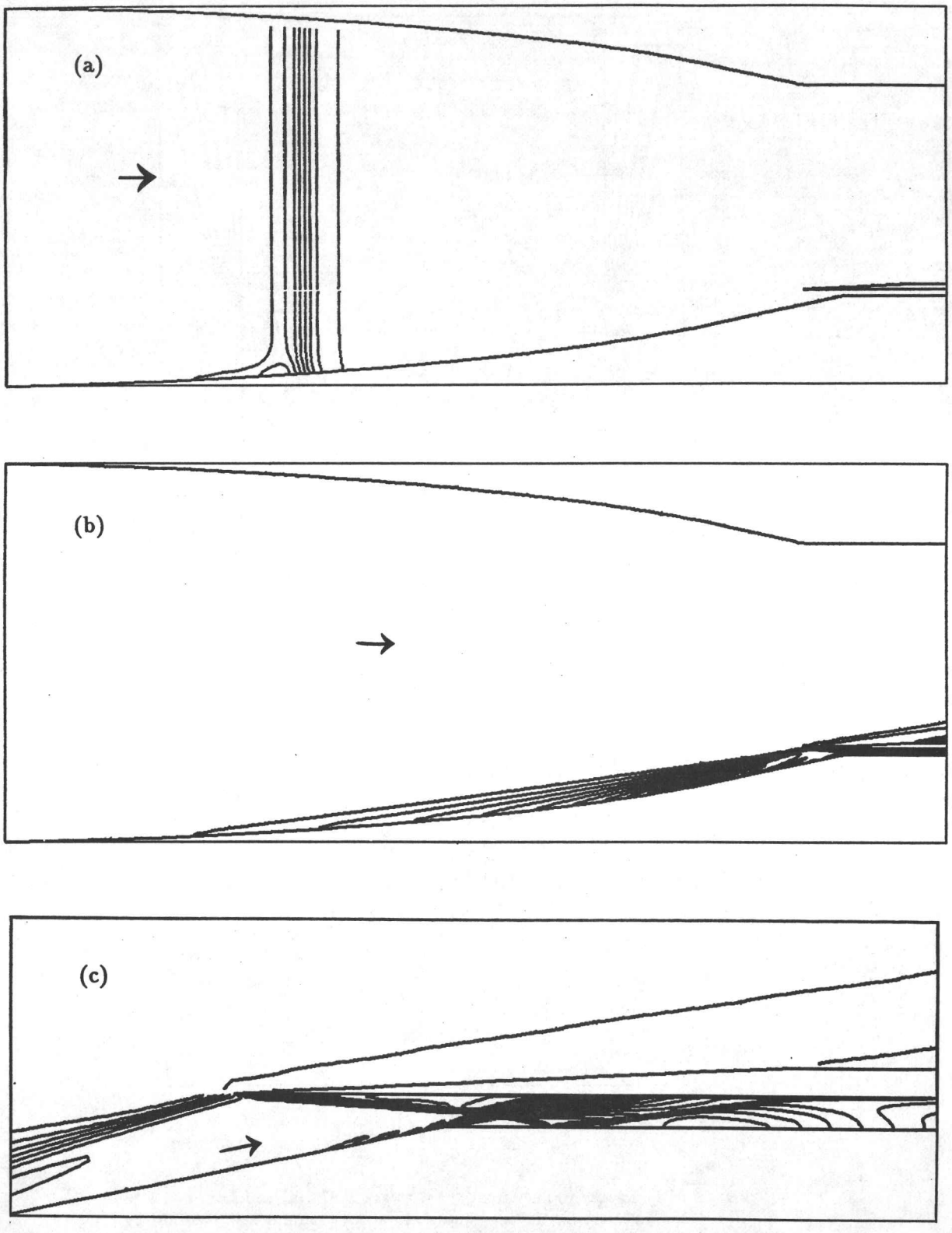

Fig. 11 Contours of constant density at $t = 1.2$ (a), at $t = 4.8$ (b), and at $t = 4.8$ with increased resolution (c), for Mach-8.4 flow from right into a spike inlet obtained using implicit time-stepping with 'minmod' and 'superbee' compression parameters set to 0.75 and one, respectively.

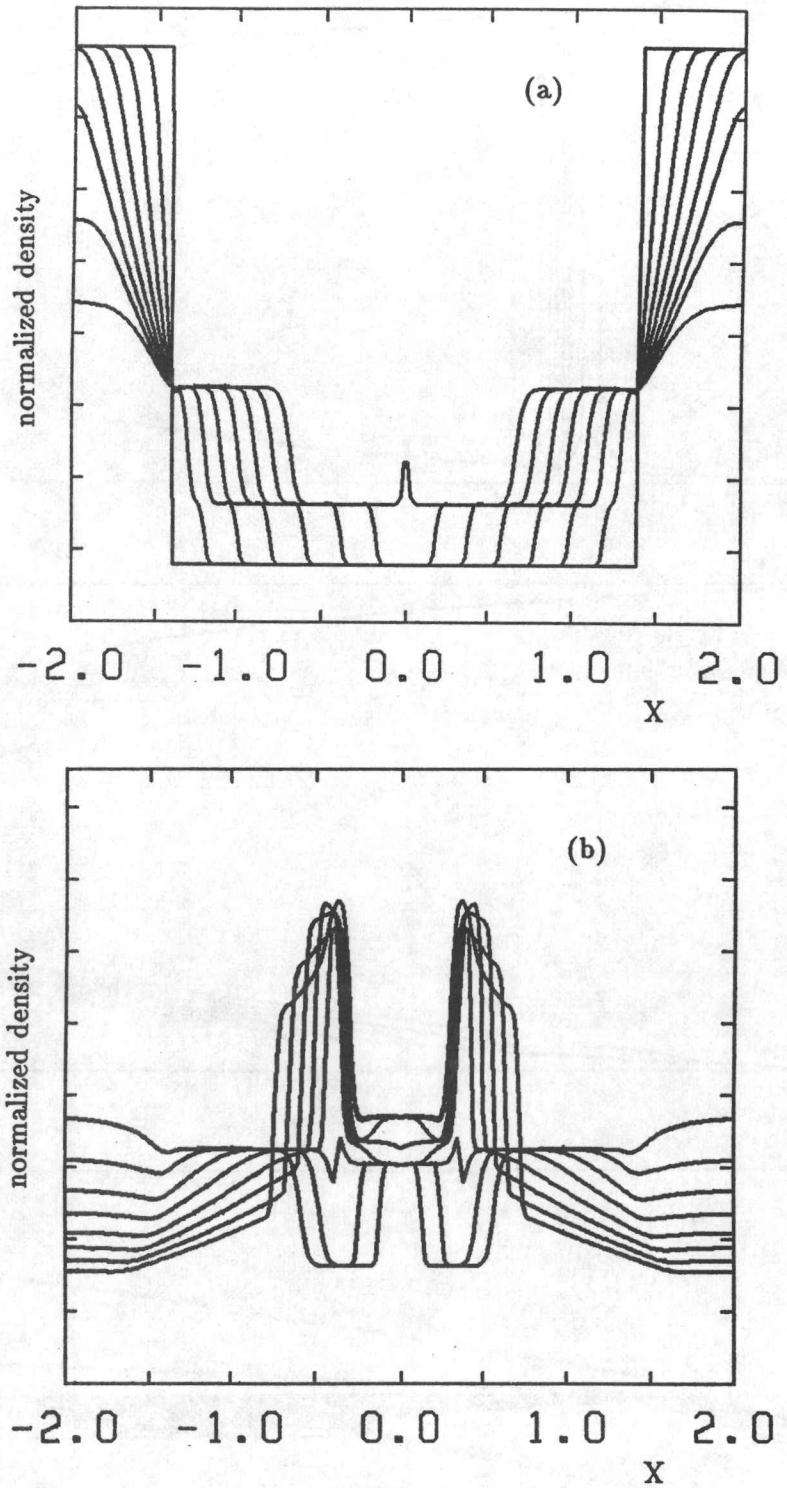

Fig. 12 ST2: Density profiles from $t = 0$ to $t = 0.875$ (a) and from $t = 1$ to $t = 1.875$ (b) for the one-dimensional shock-tube problem, obtained by using the TVD-MacCormack scheme with 'minmod' and 'superbee' compression parameters set to 1 and 1.25, respectively. Approximate time intervals between profiles is $\Delta t = 0.125$. Calculations were performed on a 200-cell grid.

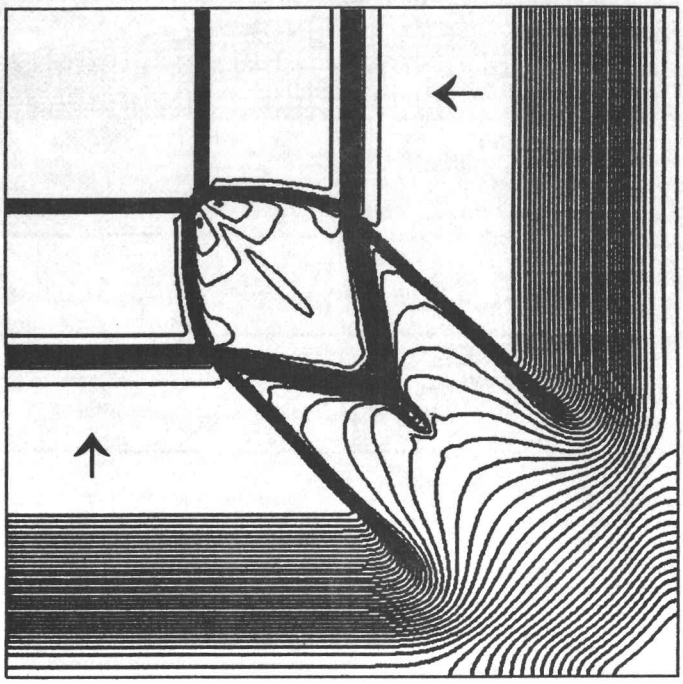

Fig. 13 SQR3: Contours of constant density for the 'shock-box' problem at $t = 0.5625$, just after the rarefaction wave has reflected off the solid walls of the box, obtained with 'minmod' and 'superbee' compression parameters set to 0.75 and 1.25, respectively. Computations were done with a 200-cell by 200-cell grid using the explicit TVD-MacCormack scheme.

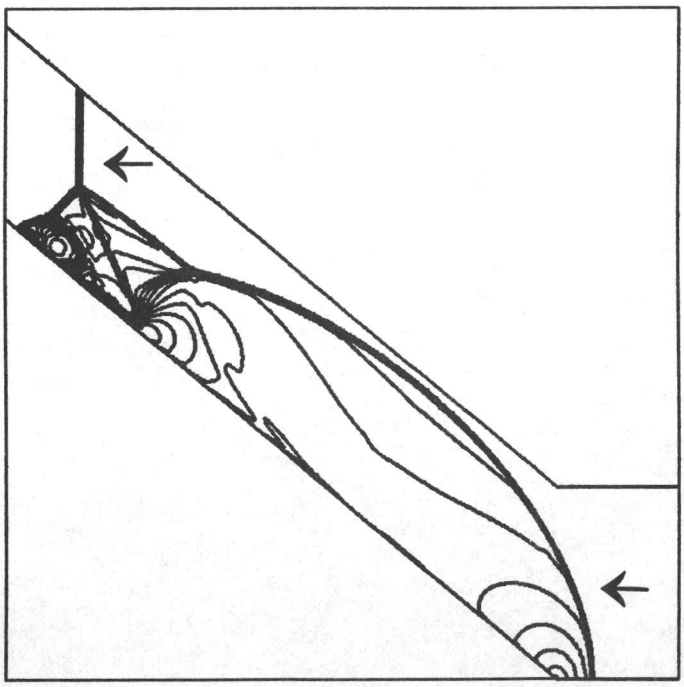

Fig. 14 WEDGE3: Contours of constant density for the Mach-3.72 shock incident from the right on a wedge, obtained using the explicit TVD-MacCormack scheme with 'minmod' and 'superbee' compression parameters set to 0.75 and 1.25, respectively.

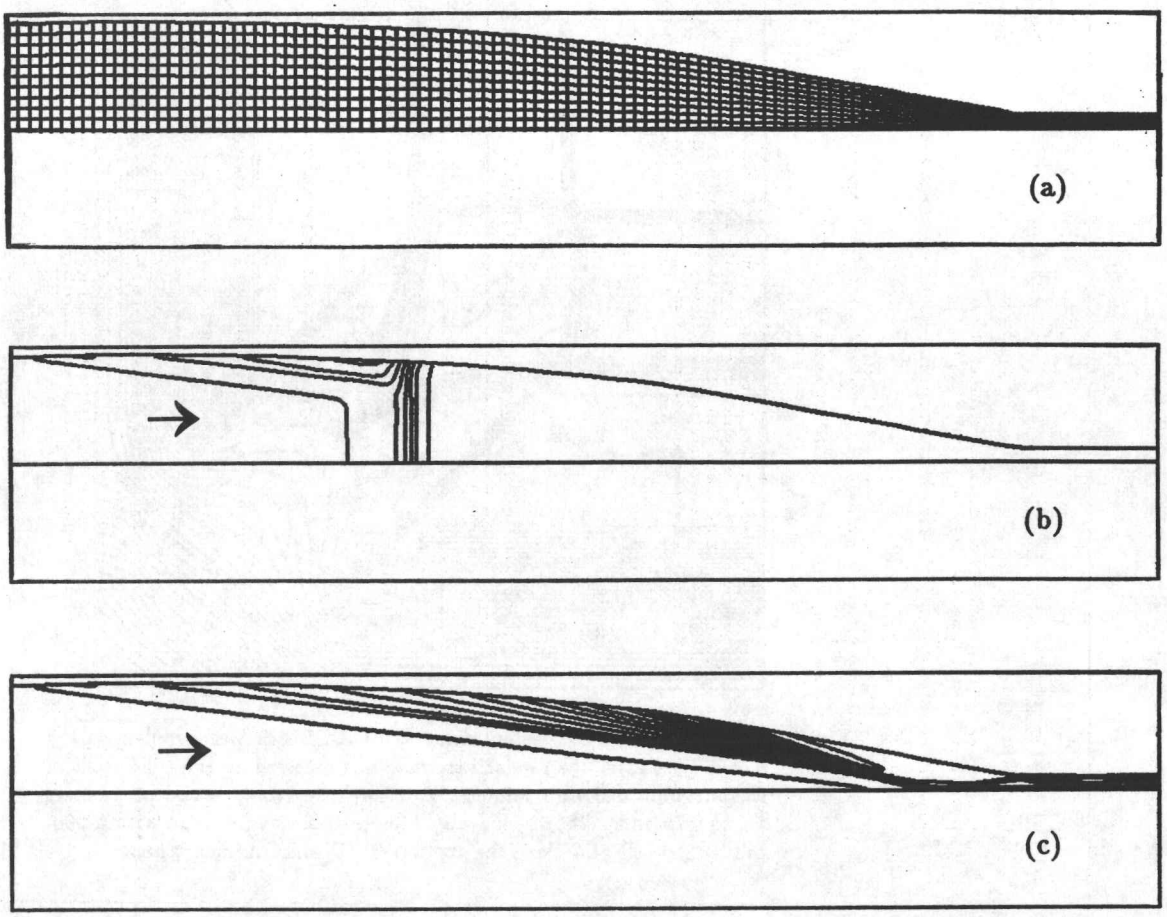

Fig. 15 PM3: Grid for Mach-8.4 flow from right into the Prandtl-Meyer inlet (a), and contours of constant density at $t = 1.2$ (b), at $t = 4.2$ (c), obtained using the explicit TVD-MacCormack scheme with 'minmod' and 'superbee' compression parameters both set to one. Only every fourth grid line is shown.

UTIAS Report No. 335

University of Toronto, Institute for Aerospace Studies (UTIAS)
4925 Dufferin Street, Downsview, Ontario, Canada, M3H 5T6

PREDICTION OF TWO-DIMENSIONAL TIME-DEPENDENT GASDYNAMIC FLOWS FOR HYPERSONIC STUDIES

Hawken, D. F. and Gottlieb, J. J.

1. TVD 2. Total variation diminishing 3. Flux limiting 4. Hypersonic flow

I. Hawken, D. F., Gottlieb, J. J. II. UTIAS Report No. 335

Work on the development of an efficient and accurate computer code for the prediction of hypersonic flows within model hypersonic inlets is reported, and numerical results for some test problems are presented. This report summarizes the finite-difference technique and total variation diminishing (TVD) scheme with Roe's approximate Riemann solver, which are incorporated into the code, in order to predict nonstationary planar and axisymmetric flows with steep shocks and thin slip streams on two-dimensional grids having multiple connected domains.

Available copies of this report are limited. Return this card to UTIAS, if you require a copy.

UTIAS Report No. 335

University of Toronto, Institute for Aerospace Studies (UTIAS)
4925 Dufferin Street, Downsview, Ontario, Canada, M3H 5T6

PREDICTION OF TWO-DIMENSIONAL TIME-DEPENDENT GASDYNAMIC FLOWS FOR HYPERSONIC STUDIES

Hawken, D. F. and Gottlieb, J. J.

1. TVD 2. Total variation diminishing 3. Flux limiting 4. Hypersonic flow

I. Hawken, D. F., Gottlieb, J. J. II. UTIAS Report No. 335

Work on the development of an efficient and accurate computer code for the prediction of hypersonic flows within model hypersonic inlets is reported, and numerical results for some test problems are presented. This report summarizes the finite-difference technique and total variation diminishing (TVD) scheme with Roe's approximate Riemann solver, which are incorporated into the code, in order to predict nonstationary planar and axisymmetric flows with steep shocks and thin slip streams on two-dimensional grids having multiple connected domains.

Available copies of this report are limited. Return this card to UTIAS, if you require a copy.

UTIAS Report No. 335

University of Toronto, Institute for Aerospace Studies (UTIAS)
4925 Dufferin Street, Downsview, Ontario, Canada, M3H 5T6

PREDICTION OF TWO-DIMENSIONAL TIME-DEPENDENT GASDYNAMIC FLOWS FOR HYPERSONIC STUDIES

Hawken, D. F. and Gottlieb, J. J.

1. TVD 2. Total variation diminishing 3. Flux limiting 4. Hypersonic flow

I. Hawken, D. F., Gottlieb, J. J. II. UTIAS Report No. 335

Work on the development of an efficient and accurate computer code for the prediction of hypersonic flows within model hypersonic inlets is reported, and numerical results for some test problems are presented. This report summarizes the finite-difference technique and total variation diminishing (TVD) scheme with Roe's approximate Riemann solver, which are incorporated into the code, in order to predict nonstationary planar and axisymmetric flows with steep shocks and thin slip streams on two-dimensional grids having multiple connected domains.

Available copies of this report are limited. Return this card to UTIAS, if you require a copy.

UTIAS Report No. 335

University of Toronto, Institute for Aerospace Studies (UTIAS)
4925 Dufferin Street, Downsview, Ontario, Canada, M3H 5T6

PREDICTION OF TWO-DIMENSIONAL TIME-DEPENDENT GASDYNAMIC FLOWS FOR HYPERSONIC STUDIES

Hawken, D. F. and Gottlieb, J. J.

1. TVD 2. Total variation diminishing 3. Flux limiting 4. Hypersonic flow

I. Hawken, D. F., Gottlieb, J. J. II. UTIAS Report No. 335

Work on the development of an efficient and accurate computer code for the prediction of hypersonic flows within model hypersonic inlets is reported, and numerical results for some test problems are presented. This report summarizes the finite-difference technique and total variation diminishing (TVD) scheme with Roe's approximate Riemann solver, which are incorporated into the code, in order to predict nonstationary planar and axisymmetric flows with steep shocks and thin slip streams on two-dimensional grids having multiple connected domains.

Available copies of this report are limited. Return this card to UTIAS, if you require a copy.